Published by
NIGERIAN SOCIETY OF PHYSICAL SCIENCES
Available online @ https://asr.nsps.org.ng/index.php/asr

African Scientific Reports 5 (2026) 536

African Scientific Reports

High-performance and economically viable La_2NiMnO_6-based carrier transport layer-free perovskite solar cell with carbon-contact feasibility: a SCAPS-1D analysis

Peverga Rex Jubu[a,b,*], Akache Nathan-Abutu[b], Francis Aungwa[b], Chijioke Amakom[a,c], Izuchukwu Kenneth Nwokolo[a], Aaron Opeyemi Aransiola[a,d], Kufre I. Udofia[a,e], John Ojinere Anyanwu[a], Dehiin Donald Hile[b,f], Madan Mohan Gururani[g], Dooshima Judith Mtsor[b], Emeka Emmanuel Oguzie[a,h,**]

[a]*Africa Centre of Excellence in Future Energies and Electrochemical System (ACE-FUELS), Federal University of Technology Owerri (FUTO), P.M.B. 1526 Owerri, Imo State, Nigeria*
[b]*Department of Industrial Physics, Joseph Sarwuan Tarka University Makurdi (Federal University of Agriculture Makurdi), P.M.B. 2373, Makurdi, Benue State, Nigeria*
[c]*Department of Physics, Federal University of Technology Owerri (FUTO), P.M.B. 1526 Owerri, Imo State, Nigeria*
[d]*Department of Electronic and Electrical Engineering, Obafemi Awolowo University, Ile-Ife, Nigeria*
[e]*Department of Physics, Akwa Ibom State University, Akwa Ibom State, Nigeria*
[f]*Department of Physics, University of Zululand, Kwadlangezwa 3886, South Africa*
[g]*Department of Physics, Moti Ram Babu Ram Government Post Graduate College, Haldwani, Uttarakhand, India*
[h]*Department of Chemistry, Federal University of Technology Owerri, Imo State, Nigeria*

Abstract

Carrier transport layers (CTLs) play a crucial role in conventional perovskite solar cells (PSCs) by aiding charge extraction. However, their involvement increases fabrication complexity, production cost, and potential instability. In this work, a simplified and economically viable CTL-free PSC configuration of FTO/La_2NiMnO_6/Au is proposed and systematically investigated using SCAPS-1D numerical simulation. Lanthanum nickel manganese oxide (La_2NiMnO_6) perovskite, an ambipolar absorber, is demonstrated to effectively perform both light absorption and charge transport without the need for auxiliary transport materials. Through systematic optimization of absorber thickness, defect density, electron capture cross-section, and resistive losses, a high power conversion efficiency (PCE) of 30.58% is recorded under standard illumination conditions, significantly outperforming previously reported single-absorber La_2NiMnO_6-based devices. The optimized device demonstrates strong defect tolerance, excellent carrier mobility balance, and robust thermal stability. Moreover, replacing the Au back contact with carbon (FTO/La_2NiMnO_6/C) yields a comparable PCE of 30.34%, confirming the potential for low-cost and scalable device fabrication. These results highlight the feasibility of eliminating CTLs in appropriately engineered devices and establish La_2NiMnO_6 as a promising material for next-generation, structure-simplified, and high-efficiency photovoltaic technologies.

DOI: 10.46481/asr.2026.5.2.536

Keywords: Perovskite solar cells, La_2NiMnO_6, Carrier transport layer-free, SCAPS-1D, Carbon contact.

Article History:
Received: 08 May 2026
Received in revised form: 15 June 2026
Accepted for publication: 16 June 2026
Available online: 15 July 2026

*Corresponding author Tel. No.: +234-703-901-7590.
**Corresponding author Tel. No.: +234-803-702-6581.
Email addresses: peverga.jubu@uam.edu.ng (Peverga Rex Jubu), emeka.oguzie@futo.edu.ng (Emeka Emmanuel Oguzie)

1. Introduction

Perovskite solar cells (PSCs) have become one of the most promising photovoltaic technologies because of their high power conversion efficiency (PCE), low-temperature fabrication, and potential for inexpensive large-scale production. Since the first report of an organometal halide PSC with a PCE of 3.8% in 2009, PSCs have undergone notable development, achieving certified efficiencies up to 27% in single-junction photovoltaic devices and approaching the performance of crystalline silicon solar cells [1–5]. Despite these advances, progress toward commercialization still requires solutions to challenges associated with device cost, fabrication complexity, and long-term stability. In particular, carrier transport layers (CTLs), namely electron transport layers (ETLs) and hole transport layers (HTLs), contribute substantially to fabrication cost and may introduce additional interfacial recombination and degradation pathways. Therefore, simplified CTL-free PSC configurations based on ambipolar absorbers have attracted growing interest as a route toward efficient, stable, and economically viable ph1otovoltaic devices [6–9].

Conventional PSCs rely on ETL and HTL stacks. However, typical CTLs, especially oxide transport layers, may require high-temperature processing, and some HTLs are expensive. CTLs can also participate in instability pathways, including interfacial reactions and ion or metal migration. Eliminating one or both CTLs can therefore improve scalability and cost effectiveness by reducing coating steps, energy use, processing time, and materials cost [6, 7, 10]. Commercial viability can also be improved through simple device structures that eliminate either the ETL or the HTL, or both CTLs, and that use carbon electrodes as an additional low-cost strategy [11]. Identifying the most suitable perovskite absorber is essential because not all perovskites can provide reasonable PCE without at least one CTL. Absorbers with ambipolar-like behavior are the most suitable candidates because they possess relatively high and balanced electron and hole mobilities that can support carrier transport without auxiliary CTLs.

To date, relatively little attention has been given to CTL-free PSC designs, and only a few reports are available in the literature [1, 6, 12], although such designs are structurally simple and potentially cost-effective. Numerous reports are available for ETL-free cells [7, 13–15], with theoretical PCE values exceeding 20%, and for HTL-free devices [16, 17]. For CTL-free structures, experimental PCE values have gradually increased: 0.88% in 2012 and 3.11% in 2020 for single-perovskite-layer cells; 8.08% in 2019 for a homo-bilayer; 10.30% in 2020 for a gradient layer; and 16.52% in 2022 for a hetero-bilayer [18]. Theoretical studies have also reported PCE values of approximately 12.0% for CTL-free designs [6, 10].

The high experimental PCE of 16.52% for a CTL-free architecture was achieved using a hetero-bilayer device, FTO/$FAPbI_3$/$MAPbI_3$/Au [18]. However, using two different perovskite materials does not substantially reduce cost and can introduce interface defects that promote recombination and performance degradation. Therefore, identifying a single perovskite absorber that performs well without an ETL or HTL would provide a simpler and more cost-effective design. Lanthanum nickel manganese oxide (La_2NiMnO_6) is a promising absorber because it is a lead-free semiconducting double perovskite with a favorable band gap of 1.0–1.4 eV, useful optical absorption, and suitable charge-transport and defect-tolerance characteristics [19–21]. PSCs using La_2NiMnO_6 absorbers have reported high PCE values of 20.18% [22], 29.20% [23], 25.44% [24], and 22.0% [25] with transport materials such as TiO_2, WS_2, SnO_2, ZnO, Spiro-OMeTAD, CFTS, MoO_3, and Cu_2O.

This study uses SCAPS-1D software to evaluate the photovoltaic behavior of the proposed FTO/La_2NiMnO_6/Au CTL-free device. Performance optimization is achieved by controlling absorber thickness, bulk defect density, electron capture cross-section, and resistive losses. The optimized device records a superior PCE, outperforming reported single-absorber La_2NiMnO_6-based PSCs that employ CTLs. To investigate a more cost-effective design, the FTO/La_2NiMnO_6/C device with a carbon back contact is also evaluated. This work is intended to stimulate further interest in CTL-free PSC designs.

2. Materials and methods

2.1. Numerical simulation

The operation of SCAPS-1D is described by a set of fundamental equations: the Poisson equation, carrier continuity equations, and drift-diffusion relations, as shown in Eqs. (1)–(5) [21, 26, 27].

$$\frac{d}{dx}\left[\varepsilon(x)\frac{d\varphi}{dx}\right] = e\left[p(x) - n(x) + N_D^+ - N_A^- + p_i(x) - n_i(x)\right], \tag{1}$$

$$-\frac{\partial J_n}{\partial x} - Z_n = \frac{\partial n}{\partial t} - H, \tag{2}$$

$$-\frac{\partial J_p}{\partial x} - Z_p = \frac{\partial p}{\partial t} - H, \tag{3}$$

where φ represents the electrostatic potential, e is the elementary charge, and n and p denote the concentrations of free electrons and holes, respectively. N_D^+ and N_A^- are the densities of ionized donor and acceptor impurities, respectively. The terms n_i and p_i describe trapped electron and hole concentrations associated with defect states. The dielectric permittivity, ε, characterizes the ability of the material to respond to electric fields and plays a crucial role in determining internal electrostatics.

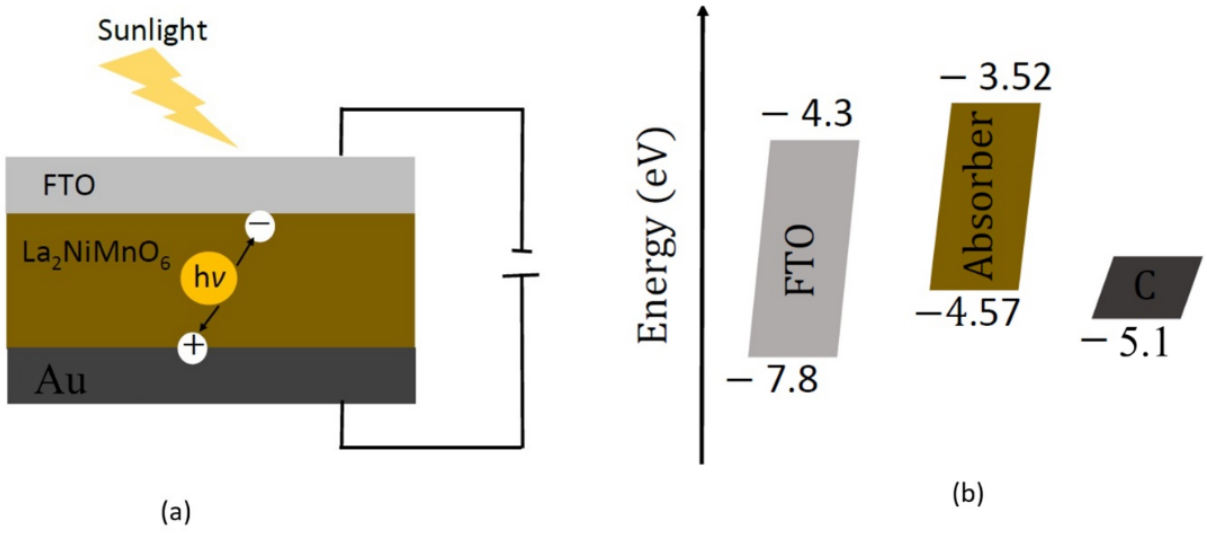

Figure 1: (a) Schematic illustration of the CTL-free PSC and (b) energy-level diagram.

The continuity equations in Eqs. (2) and (3) describe the balance among charge-carrier generation, recombination, and transport within the device. In these equations, J_n and J_p designate electron and hole current densities, respectively; Z_n and Z_p represent recombination rates; H is the carrier-generation rate; and t is time. Charge-carrier transfer is modeled using the drift-diffusion expressions in Eqs. (4) and (5).

$$J_n = \left(-\frac{\mu_n n}{e}\right)\frac{\partial E_{Fn}}{\partial x}, \tag{4}$$

$$J_p = \left(-\frac{\mu_p p}{e}\right)\frac{\partial E_{Fp}}{\partial x}, \tag{5}$$

where μ_n and μ_p are electron and hole mobilities, respectively, and E_{Fn} and E_{Fp} are the quasi-Fermi levels for electrons and holes.

In this work, CTL-free solar-cell structures were modeled using fluorine-doped tin oxide (FTO) as the front contact, whereas Au with a work function of 5.1 eV was used as the back contact for effective charge collection and transfer to the external circuit. The perovskite absorbers were used as the light-absorbing and electron–hole-pair-generating layers. Realistic simulation conditions were used to represent laboratory and environmental conditions. The standard AM 1.5 solar spectrum with an intensity of 100 $\mathrm{mW/cm^2}$ was used, and the operating temperature was fixed at 25 °C (300 K). The selection of materials and their electronic properties was guided by established reports. The input parameters are summarized in Tables 1–4. Critical variables, including layer thickness, bulk defect density, series and shunt resistances, electron capture cross-section, and back-contact work function, were systematically adjusted to optimize PSC performance.

Some acceptor carrier concentrations higher than 1.0×10^{18} $\mathrm{cm^{-3}}$ were used for selected absorbers to avoid convergence failure and to allow simulated carrier separation and transfer to the appropriate electrodes. Such concentrations may be difficult to realize experimentally and are therefore treated as physical constraints in interpreting the screening results.

2.2. Working principle of the CTL-free PSC

The working principle of the CTL-free PSC follows a simple mechanism. The FTO anode acts as the transparent conducting front electron-collecting contact. Its transparency allows incident light to reach the absorber layer with minimal parasitic absorption in the visible spectrum. The La_2NiMnO_6 absorber serves as both the light absorber and ambipolar transport medium, while Au acts as the high-work-function back hole-collecting contact. Under illumination, the absorber simultaneously serves as absorber, electron transport channel, and hole transport path, enabling operation without CTLs. The FTO/La_2NiMnO_6 front interface forms an electron-selective quasi-ohmic or weak Schottky contact that enables downward band bending and favors electron extraction. The Au/La_2NiMnO_6 interface forms a hole-selective back contact with upward band bending that favors hole extraction to the external circuit. Incident photons pass through the transparent FTO and are absorbed in the La_2NiMnO_6 layer, generating electron–hole pairs. A built-in electric field is created by the work-function difference between the FTO and Au contacts, as shown in Eq. (6) [42].

$$V_{bi} = \frac{\varphi_{\mathrm{Au}} - \varphi_{\mathrm{FTO}}}{e}, \tag{6}$$

where V_{bi} is the built-in potential, φ_{Au} is the work function of Au, φ_{FTO} is the work function of FTO, and e is the elementary charge. The field transfers electrons to FTO and holes to Au without requiring separate transport materials. Therefore, the PSC can be described as a self-selective Schottky-junction photovoltaic device.

Table 1: Fundamental physical parameters employed in the simulations involving La_2NiMnO_6, Cs_2TiBr_6, $MAPbI_3$, $CsSnI_3$, and $CsPbBr_3$.

Parameter	FTO [28]	La_2NiMnO_6 [21, 29]	Cs_2TiBr_6 [30]	$MAPbI_3$ [16]	$CsSnI_3$ [31]	$CsPbBr_3$ [28]
Thickness (μm)	0.5	0.8	0.8	0.8	0.8	0.8
E_g (eV)	3.5	1.05	1.8	1.55	1.3	2.3
χ (eV)	4.3	3.52	4.47	6.50	3.6	3.6
ε_r	9.0	3.50	10.0	3.90	9.93	6.5
N_C (cm^{-3})	2.2×10^{18}	1.0×10^{18}	6.0×10^{19}	2.2×10^{18}	1.0×10^{19}	4.94×10^{17}
N_V (cm^{-3})	1.8×10^{19}	1.0×10^{18}	2.0×10^{19}	2.2×10^{18}	1.0×10^{18}	8.47×10^{18}
μ_n ($cm^2\ V^{-1}\ s^{-1}$)	20.0	22	4.4	2.0	1.5×10^3	4.5×10^3
μ_p ($cm^2\ V^{-1}\ s^{-1}$)	10.0	22	2.5	2.0	5.85×10^2	4.5×10^3
eV_{th} (cm/s)	1×10^7	1×10^7	1×10^7	1×10^7	1×10^7	1×10^7
hV_{th} (cm/s)	1×10^7	1×10^7	1×10^7	1×10^7	1×10^7	1×10^7
N_D (cm^{-3})	2×10^{19}	0	0	0	0	0
N_A (cm^{-3})	0	1×10^{12}	1×10^{19}	1×10^{16}	1×10^{12}	1×10^{16}
N_t (cm^{-3})	1×10^{15}	1×10^{17}	1×10^{14}	1×10^{14}	1×10^{17}	1×10^{14}
σ_e (cm^2)	1×10^{-15}	1×10^{-19}	1×10^{-19}	1×10^{-19}	1×10^{-19}	1×10^{-19}
σ_h (cm^2)	1×10^{-15}	1×10^{-15}	1×10^{-15}	1×10^{-15}	1×10^{-15}	1×10^{-15}

Table 2: Fundamental physical parameters employed in the simulations involving $MASnBr_3$, $MAGeI_3$, $CsSnCl_3$, $Cs_2AgBiCl_6$, $BaZrSe_3$, and $SrZrS_3$.

Parameter	$MASnBr_3$ [32]	$MAGeI_3$ [33]	$CsSnCl_3$ [34]	$Cs_2AgBiCl_6$ [35]	$BaZrSe_3$ [36]	$SrZrS_3$ [37, 38]
Thickness (μm)	0.8	0.8	0.8	0.8	0.8	0.8
E_g (eV)	1.3	1.9	1.52	2.41	1.01	1.52
χ (eV)	4.17	3.98	3.95	4.2	4.5	4.8
ε_r	10.0	10.0	29.4	5.0	10.0	10.0
N_C (cm^{-3})	1.8×10^{18}	1.0×10^{16}	1.8×10^{18}	1.0×10^{20}	2.2×10^{18}	4.6×10^{18}
N_V (cm^{-3})	2.2×10^{18}	1.0×10^{15}	2.2×10^{18}	1.0×10^{20}	1.8×10^{19}	1.0×10^{19}
μ_n ($cm^2\ V^{-1}\ s^{-1}$)	1.6	1.62×10^2	2.0	7.0	11.3	18.77
μ_p ($cm^2\ V^{-1}\ s^{-1}$)	1.6	1.01×10^2	2.0	9.0	5.8	6.81
eV_{th} (cm/s)	1×10^7	1×10^7	1×10^7	1×10^7	1×10^7	1×10^7
hV_{th} (cm/s)	1×10^7	1×10^7	1×10^7	1×10^7	1×10^7	1×10^7
N_D (cm^{-3})	0	0	0	0	0	0
N_A (cm^{-3})	1×10^{22}	1×10^{16}	1×10^{22}	1×10^{16}	1×10^{22}	1×10^{16}
N_t (cm^{-3})	1×10^{17}	1×10^{14}	1×10^{17}	1×10^{14}	1×10^{14}	1×10^{14}
σ_e (cm^2)	1×10^{-19}	1×10^{-19}	1×10^{-19}	1×10^{-19}	1×10^{-19}	1×10^{-19}
σ_h (cm^2)	1×10^{-15}	1×10^{-15}	1×10^{-15}	1×10^{-15}	1×10^{-15}	1×10^{-15}

3. Results and discussion

3.1. Photovoltaic performance of the prototype PSCs and selection of the La_2NiMnO_6*-based device*

To justify the focus on La_2NiMnO_6, several perovskite absorbers were investigated in the CTL-free design. Table 5 presents the photovoltaic performance of the prototype devices employing different absorber layers.

The selection of an appropriate perovskite absorber for further optimization in CTL-free PSCs must go beyond identifying the prototype device with the highest PCE. It should be based on PCE, physical realism of input parameters, bulk defect tolerance, and potential for further performance improvement. In this device series, the FTO/La_2NiMnO_6/Au device stands out as the most suitable candidate for comprehensive optimization, as shown in Table 5 and Figure 2.

First, the La_2NiMnO_6-based PSC demonstrated a high baseline PCE of 22.30%, with a high J_{SC} of 43.91 mA/cm^2 and a reasonable V_{OC} of 0.88 V. This performance was achieved under a realistic acceptor concentration, $N_A = 10^{12}\ cm^{-3}$. This is a key advantage over several high-performing absorbers, such as $MASnBr_3$, $CsSnCl_3$, and $FAPbI_3$, whose PCE values depend on extremely high and often impractical doping levels of $N_A = 10^{22}\ cm^{-3}$. Such conditions may lead to degeneracy effects, elevated ionized impurity scattering, and instability, thereby limiting practical applicability. In contrast, the La_2NiMnO_6 solar cell operated efficiently within a physically reasonable carrier-density regime.

A critical strength of the La_2NiMnO_6 absorber is its high J_{SC}, which can be attributed to its relatively narrow band gap of 1.05 eV. This enables broad absorption across the solar spectrum, especially in the near-infrared region, and maximizes carrier

Table 3: Fundamental physical parameters employed in the simulations involving $CH_3NH_3SnI_3$, $MAPbBr_3$, $FASnI_3$, and $FAPbI_3$.

Parameter	$CH_3NH_3SnI_3$ [39]	$MAPbBr_3$ [10]	$FASnI_3$ [23, 34]	$FAPbI_3$ [40]
Thickness (μm)	0.8	0.8	0.8	0.8
E_g (eV)	1.51	2.3	1.45	1.51
χ (eV)	4.0	3.6	4.0	4.0
ε_r	6.0	6.5	8.2	6.6
N_C (cm^{-3})	1.2×10^{19}	2.2×10^{19}	1.0×10^{18}	1.2×10^{19}
N_V (cm^{-3})	2.9×10^{18}	1.8×10^{18}	1.0×10^{18}	2.9×10^{18}
μ_n ($cm^2\ V^{-1}\ s^{-1}$)	2.7	20	22	2.7
μ_p ($cm^2\ V^{-1}\ s^{-1}$)	1.8	20	22	1.8
eV_{th} (cm/s)	1×10^7	1×10^7	1×10^7	1×10^7
hV_{th} (cm/s)	1×10^7	1×10^7	1×10^7	1×10^7
N_D (cm^{-3})	0	0	0	0
N_A (cm^{-3})	1×10^{20}	1×10^{16}	1×10^{16}	1×10^{16}
N_t (cm^{-3})	1×10^{14}	1×10^{14}	1×10^{14}	1×10^{14}
σ_e (cm^2)	1×10^{-19}	1×10^{-19}	1×10^{-19}	1×10^{-19}
σ_h (cm^2)	1×10^{-15}	1×10^{-15}	1×10^{-15}	1×10^{-15}

Table 4: Defect interface parameters [28, 41].

Parameter	Absorber	ETL/absorber interface	Absorber/HTL interface
Defect type	Neutral	Neutral	Neutral
Cross section for electrons (cm^2)	1×10^{-15}	1×10^{-19}	1×10^{-19}
Cross section for holes (cm^2)	1×10^{-15}	1×10^{-19}	1×10^{-19}
Energetic distribution	Gaussian	Single	Single
Energy level with respect to E_V (eV)	0.60	0.65	0.65
Characteristic energy (eV)	0.10	0.10	0.10

photogeneration. In CTL-free architectures, where selective charge extraction layers are absent, the absorber must exhibit ambipolar behavior to support carrier generation and transport to the electrodes. The high J_{SC} of the La_2NiMnO_6 PSC indicates that it satisfies this requirement.

Equally important is the tolerance of the La_2NiMnO_6-based device to bulk defects. The device functions satisfactorily across a wide bulk-defect-density range of 10^{14}–$10^{18}\,cm^{-3}$, unlike several other CTL-free PSCs. Defect tolerance is a key photovoltaic parameter because practical devices inevitably contain imperfections that can act as recombination centers. Materials that maintain photovoltaic output across a wide range of defect densities are inherently more robust for scalable fabrication. In contrast, absorbers such as Cs_2TiBr_6, $MAPbI_3$, $CsPbBr_3$, and $MAGeI_3$ showed low performance even at moderate defect densities of $10^{14}\,cm^{-3}$, limiting their suitability for further optimization.

Another important consideration is the balance of electron and hole mobilities in La_2NiMnO_6, $\mu_n = \mu_p = 22\,cm^2\,V^{-1}\,s^{-1}$. Balanced carrier transport is essential in CTL-free devices because there are no dedicated CTLs to selectively guide carrier flow and suppress recombination. This intrinsic transport symmetry improves charge extraction and device performance. The effect is more beneficial when the absorber has a relatively low band gap, as in La_2NiMnO_6. Low-band-gap materials absorb a wider portion of the solar spectrum, including the near-infrared region, increasing photogeneration and J_{SC} [43, 44]. This explains why $CsPbBr_3$, $MAPbBr_3$, and $FASnI_3$ can exhibit balanced mobilities but still show lower PCE values when their band gaps or defect responses are less favorable [45].

Although the La_2NiMnO_6-based prototype exhibited a lower fill factor (FF) of 57.89% than some other prototypes, this is an opportunity for optimization rather than a fundamental limitation. The FF can be improved by tuning parameters such as defect density, absorber thickness, and electron capture cross-section. In comparison, the $CsSnI_3$-based PSC exhibited a slightly higher initial PCE of 24.42% under realistic doping, but showed limited further improvement upon optimization. Thus, La_2NiMnO_6 offers a favorable combination of strong prototype performance and substantial optimization headroom.

The quantum efficiency (QE) spectrum in Figure 2 shows a near-unity response over a wide spectral range of 350–900 nm, with a sharp cutoff at 1180 nm, consistent with the 1.05 eV band gap of La_2NiMnO_6. The energy-band diagram further indicates favorable carrier selectivity, with a conduction-band offset of 0.78 eV at the FTO/absorber interface that supports electron transfer to FTO, whereas a large valence-band offset of 3.23 eV blocks holes. Conversely, the Au back contact forms an effective hole-collecting contact and suppresses electron back transfer.

Table 5: Photovoltaic performance of the prototype carrier transport layer-free perovskite solar cells.

Device	E_g (eV)	V_{OC} (V)	J_{SC} (mA/cm^2)	FF (%)	PCE (%)	Comment
FTO/La_2NiMnO_6/Au	1.05	0.88	43.91	57.89	22.30	High PCE and large N_t tolerance; operates under a realistic low N_A of 10^{12} cm^{-3}.
FTO/Cs_2TiBr_6/Au	1.80	0.24	17.76	61.83	2.62	Low PCE at $N_t = 10^{14}$ cm^{-3}; uses an extremely high N_A of 10^{19} cm^{-3}.
FTO/$MAPbI_3$/Au	1.55	1.41	0.11	89.88	0.13	Low PCE at $N_t = 10^{14}$ cm^{-3} and $N_A = 10^{16}$ cm^{-3}.
FTO/$CsSnI_3$/Au	1.30	0.98	34.27	72.90	24.42	High PCE and large N_t tolerance; operates under $N_A = 10^{16}$ cm^{-3}, but improves only slightly after optimization.
FTO/$CsPbBr_3$/Au	2.30	1.41	7.83	50.41	5.56	Low PCE at $N_t = 10^{14}$ cm^{-3} and $N_A = 10^{16}$ cm^{-3}.
FTO/$MASnBr_3$/Au	1.30	1.27	27.50	90.10	31.48	Large N_t tolerance, but requires extreme $N_A = 10^{22}$ cm^{-3}.
FTO/$MAGeI_3$/Au	1.90	0.92	15.57	75.11	10.76	Low PCE at $N_t = 10^{14}$ cm^{-3} and $N_A = 10^{16}$ cm^{-3}.
FTO/$CsSnCl_3$/Au	1.52	1.48	20.66	91.301	27.94	Large N_t tolerance, but requires extreme $N_A = 10^{22}$ cm^{-3}.
FTO/$Cs_2AgBiCl_6$/Au	2.41	0.45	6.39	74.44	2.15	Low PCE at $N_t = 10^{14}$ cm^{-3} and extreme $N_A = 10^{22}$ cm^{-3}.
FTO/$BaZrSe_3$/Au	1.01	0.88	23.76	78.88	16.55	Low PCE at $N_t = 10^{14}$ cm^{-3}; requires extreme $N_A = 10^{22}$ cm^{-3}.
FTO/$SrZrS_3$/Au	1.52	0.19	23.23	60.65	2.612	Low PCE at $N_t = 10^{14}$ cm^{-3} and realistic $N_A = 10^{16}$ cm^{-3}.
FTO/$MASnI_3$/Au	1.51	0.74	31.94	81.25	19.21	Appreciable performance at $N_t = 10^{14}$ cm^{-3} and $N_A = 10^{16}$ cm^{-3}.
FTO/$FAPbI_3$/Au	1.51	1.38	21.01	90.82	26.42	Large N_t tolerance, but requires extreme $N_A = 10^{22}$ cm^{-3}.
FTO/$FASnI_3$/Au	1.45	0.80	28.72	81.04	18.65	Appreciable performance at $N_t = 10^{14}$ cm^{-3} and $N_A = 10^{16}$ cm^{-3}.
FTO/$MAPbBr_3$/Au	2.3	1.30	7.80	53.54	5.43	Low PCE at $N_t = 10^{14}$ cm^{-3} and realistic $N_A = 10^{16}$ cm^{-3}.

Notes: N_t: bulk defect density; N_A: acceptor carrier concentration; PCE: power conversion efficiency.

3.2. *Effect of* La_2NiMnO_6 *absorber thickness*

The effect of absorber thickness on the photovoltaic performance of the FTO/La_2NiMnO_6/Au CTL-free device was systematically studied by varying the La_2NiMnO_6 film thickness from 0.4 to 0.9 μm. The associated trends in V_{OC}, J_{SC}, FF, and PCE in Figure 3 reveal a clear balance between optical absorption and carrier transport/recombination, which is typical of CTL-free architectures. Increasing thickness caused J_{SC} to rise monotonically from 40.79 to 44.16 mA/cm^2, attributable to improved QE in the 800–1180 nm range and enhanced carrier generation.

In contrast, V_{OC} decreased gradually from 0.91 to 0.87 V with increasing film thickness. This trend is explained by a thickness-dependent increase in bulk recombination. As absorber thickness increases, photogenerated carriers must travel longer distances to reach the contacts, raising their probability of recombination through bulk traps. The increase in recombination current reduces quasi-Fermi-level splitting and therefore lowers V_{OC}, despite improved photogeneration. The V_{OC} relationship is given in Eq. (7) [21, 46].

$$V_{OC} = \frac{nkT}{e} \ln\left(\frac{J_{ph}}{J_0} + 1\right), \tag{7}$$

where n is the ideality factor, J_{ph} is the photogenerated current density, J_0 is the dark saturation current density, e is the electron charge, T is temperature, and k is the Boltzmann constant.

The FF decreased systematically from 62.70% to 57.03% with increasing thickness. This behavior is expected in CTL-free PSCs, where no selective transport layers are present to assist carrier extraction. Thicker absorbers introduce longer carrier-transport paths, higher resistive losses, and greater recombination under forward bias, degrading diode quality and reducing J–V curve squareness. The combined effect of increasing J_{SC} and declining V_{OC} and FF produced optimal PCE values at intermediate thicknesses. The maximum PCE of 23.3% was achieved at 0.4 and 0.5 μm, after which PCE declined to 21.94% at 0.9 μm. Thus, a thickness of 0.4 μm was selected as the optimal balance between optical absorption and carrier collection. The PCE and FF are defined in Eqs. (8) and (9) [47, 48].

$$PCE = \frac{V_{OC} \times J_{SC} \times FF}{P_{in}}, \tag{8}$$

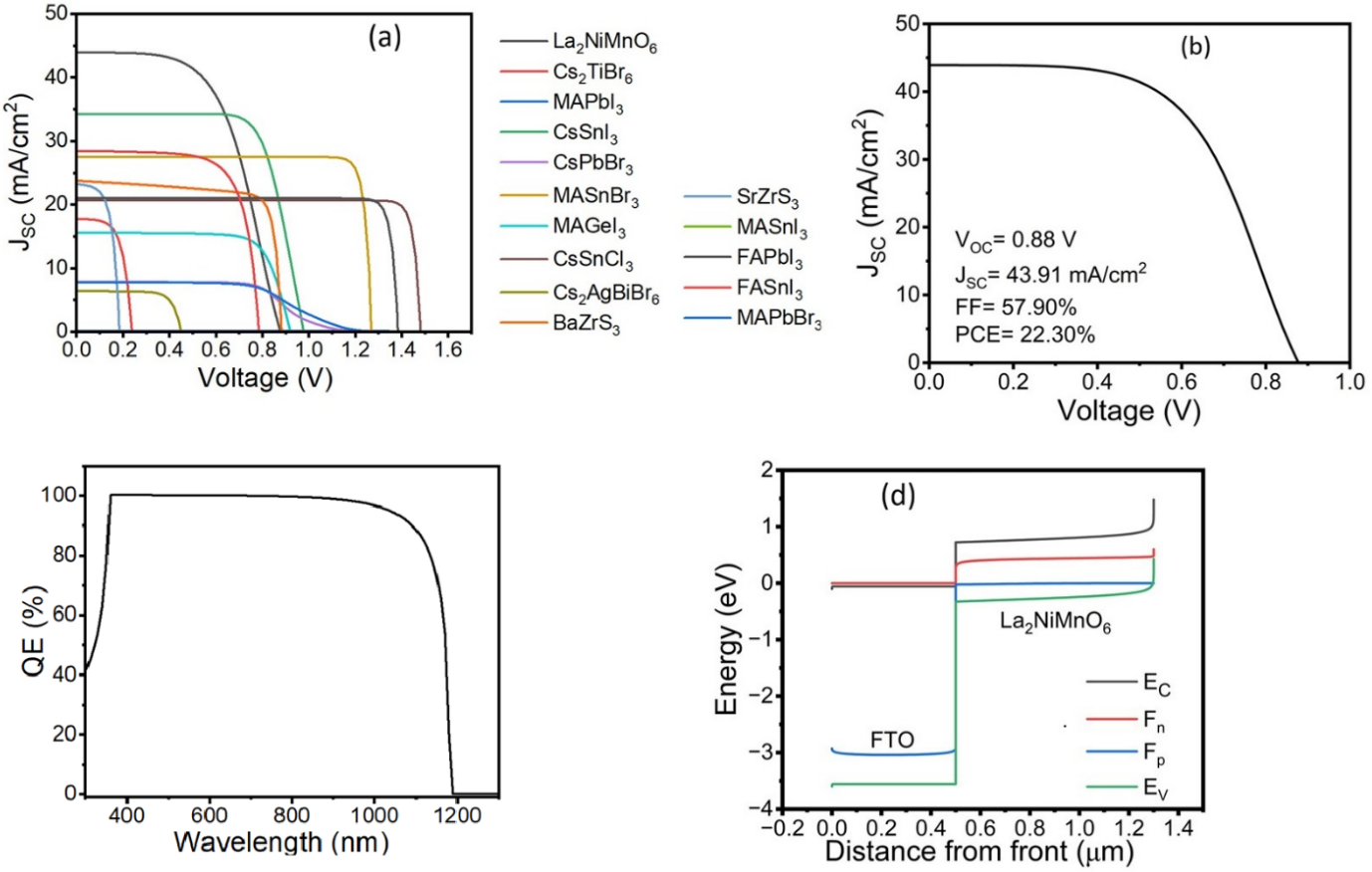

Figure 2: (a) J–V characteristics of the various prototype CTL-free PSCs, (b) isolated J–V curve of the prototype La_2NiMnO_6-based PSC, (c) QE plot of the La_2NiMnO_6-based PSC, and (d) energy-band plot of the La_2NiMnO_6-based PSC.

$$FF = \frac{J_{\text{mmp}} \times V_{\text{mmp}}}{V_{\text{OC}} \times J_{\text{SC}}}, \tag{9}$$

where P_{in} is the incident light power density, J_{mmp} is the current at the maximum power point, and V_{mmp} is the voltage at the maximum power point.

3.3. Influence of bulk defect density

Defect density in PSCs is a key parameter because bulk traps serve as non-radiative recombination centers, limit carrier lifetime and diffusion length, and thereby reduce V_{OC}, J_{SC}, FF, and device stability [49]. Lowering bulk defect concentration improves charge transport and photovoltaic output [50] by minimizing non-radiative recombination and ion migration. The major causes of bulk defects include precursor stoichiometry imbalance, rapid or poor crystallization, intrinsic point defects such as vacancies, interstitials, and antisites, intragrain impurities, and stress-induced ion migration or trap generation during operation [51, 52].

The bulk defect density of the absorber was varied from 10^{16} to 10^{20} cm^{-3}, and its influence on photovoltaic parameters was systematically investigated. A significant decrease in V_{OC}, from 0.98 to 0.65 V, was observed with increasing defect density in Figure 4. This behavior is attributed to enhanced Shockley–Read–Hall (SRH) recombination via deep trap states, which increases the recombination current density and reduces quasi-Fermi-level splitting. The SRH recombination rate is given by Eq. (10) [42], and the carrier lifetimes are given by Eq. (11) [21, 42, 53].

$$R_{\text{SRH}}(x) = \frac{np - n_i^2}{\tau_p(n + n_1) + \tau_n(p + p_1)}, \tag{10}$$

$$\tau_n = \frac{1}{\sigma_n v_{\text{th}} N_t}, \qquad \tau_p = \frac{1}{\sigma_p v_{\text{th}} N_t}, \tag{11}$$

where $R_{\text{SRH}}(x)$ is the SRH recombination rate at depth x, n and p are electron and hole concentrations, n_i is the intrinsic carrier concentration of the absorber, τ_n and τ_p are electron and hole SRH lifetimes, n_1 and p_1 are SRH reference concentrations, v_{th} is thermal velocity, N_t is the bulk trap density, and σ_n and σ_p are electron and hole capture cross-sections, respectively.

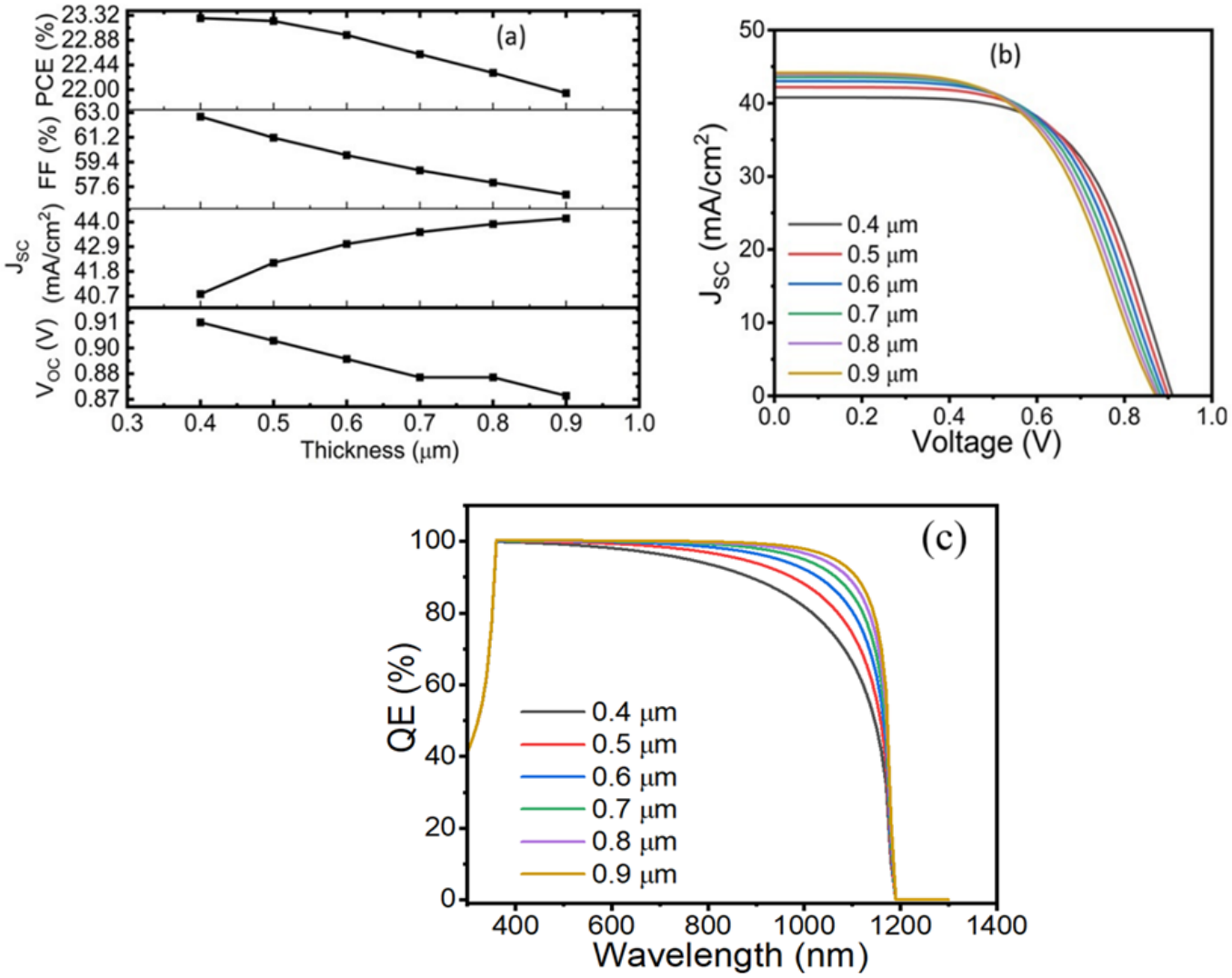

Figure 3: (a) Dependence of V_{OC}, J_{SC}, FF, and PCE on film thickness, (b) associated J–V curves, and (c) QE plots.

In contrast, J_{SC} remained nearly constant at 43.9 mA/cm^2 as defect density increased from 10^{16} to 10^{18} cm^{-3}, and it declined significantly only at very high trap density, as shown in Figures 4 and 5. This relative insensitivity to moderate defect concentrations suggests that the built-in electric field and high optical absorption of the absorber are sufficient to collect most photogenerated carriers before recombination under short-circuit conditions. However, at 10^{19} cm^{-3}, carrier lifetime becomes severely reduced, leading to incomplete charge collection and a large drop in J_{SC}.

The FF showed the strongest sensitivity to defect density, declining from 70.62% to 19.59% with increasing trap density. This steep decrease reflects a strong deterioration in diode quality due to trap-assisted recombination under forward bias. Carrier trapping, reduced mobility, and screening of the internal electric field collectively distort the J–V characteristics, causing a substantial loss of curve squareness. This effect is especially severe in CTL-free architectures because no transport layers are available to selectively extract carriers or suppress recombination near the contacts. The lower J_{SC} at the highest defect density is supported by the lower QE shown in Figure 5. The PCE decreased sharply from 30.55% to 5.43% because of the combined losses in V_{OC} and FF, confirming that trap-assisted non-radiative recombination is the dominant limiting mechanism at high trap density.

These findings suggest that a bulk defect density of approximately 10^{16} cm^{-3} is essential for preserving high quasi-Fermi-level splitting, maintaining efficient carrier transport, and achieving high device output. Unlike conventional PSCs that rely on ETLs and HTLs to mitigate recombination losses, CTL-free configurations place stronger demands on absorber quality because the absorber must simultaneously perform light harvesting and charge transport. When these requirements are satisfied, the reduction in interface-related recombination can enable performance comparable to or higher than CTL-assisted architectures.

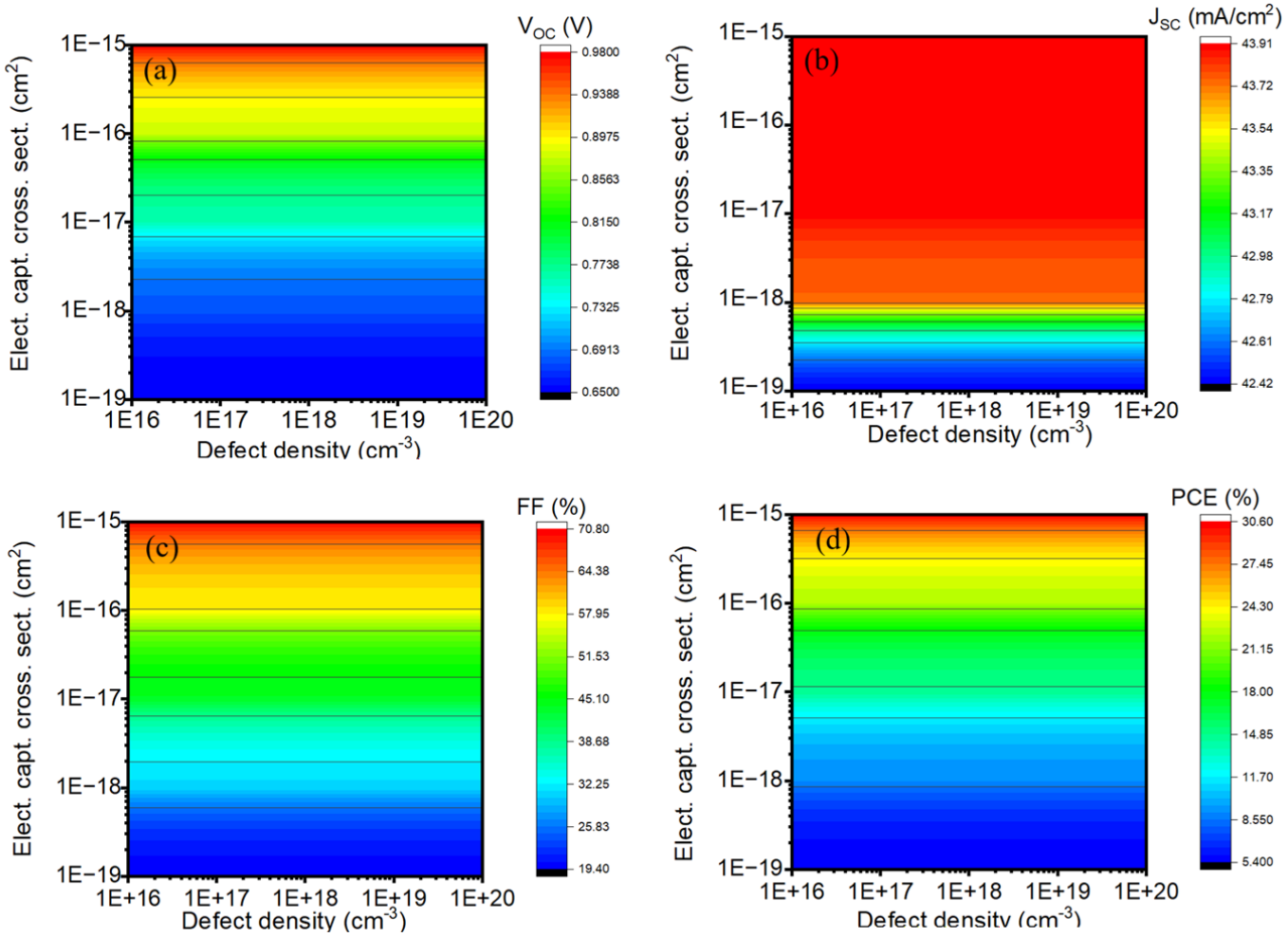

Figure 4: Contour maps showing the variation of (a) V_{OC}, (b) J_{SC}, (c) FF, and (d) PCE with defect density and electron capture cross-section in the absorber layer.

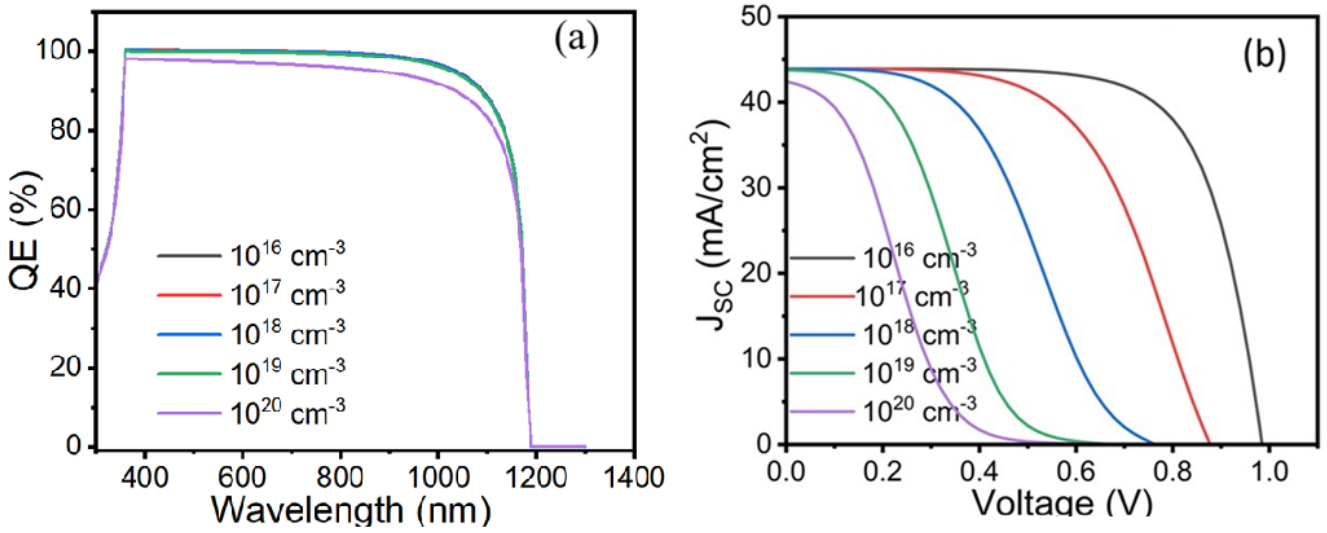

Figure 5: (a) QE plots and (b) J–V curves showing the impact of bulk defect density.

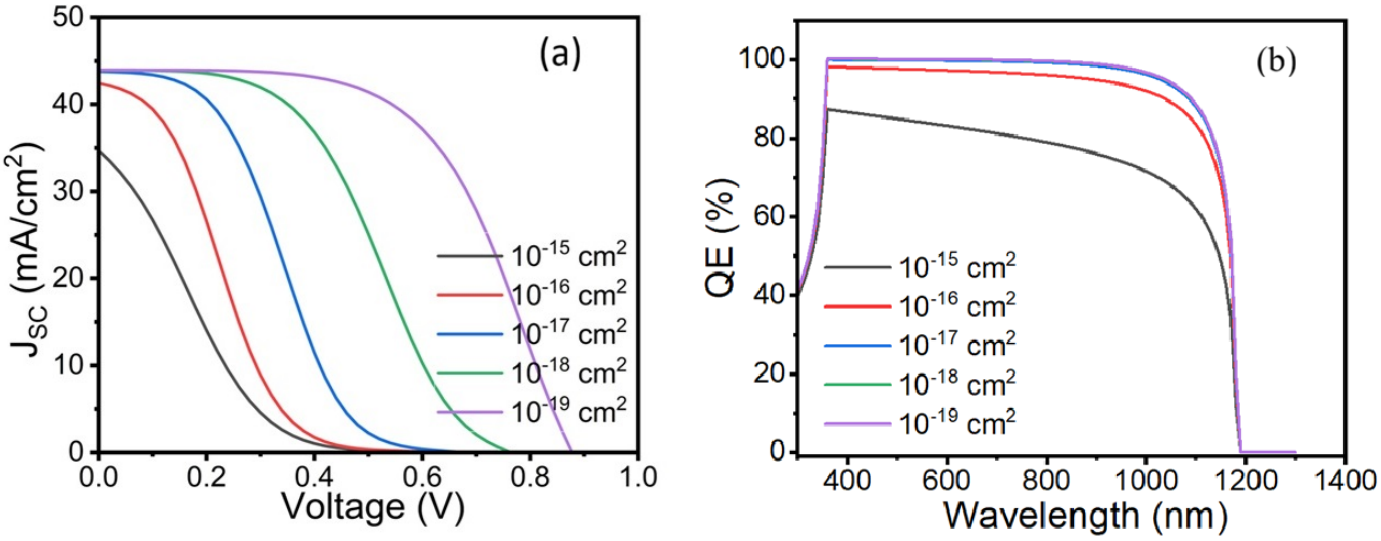

Figure 6: (a) Dependence of the J–V curves on decreasing electron capture cross-section and (b) QE plots.

3.4. Impact of electron capture cross-section in the absorber

Varying the electron capture cross-section of bulk traps from 10^{-15} to 10^{-19} cm^2 produced a significant improvement in all photovoltaic metrics. The electron capture cross-section controls how efficiently defect states capture free electrons and therefore determines the strength of SRH trap-assisted recombination in the absorber. The effective electron lifetime associated with SRH recombination follows Eq. (11). The PCE increased sharply from 3.08% to 22.30% as the electron capture cross-section decreased, as shown in Figure 4. This indicates that SRH recombination dominates device performance when the capture cross-section is large. Reducing the capture cross-section progressively restores quasi-radiative behavior by lowering J_0, which is critical in CTL-free cells that lack selective ETL/HTL layers to mitigate recombination losses.

The V_{OC} increased from 0.65 to 0.88 V as SRH recombination weakened. The FF also increased markedly from 13.64% to 57.90%, indicating improved diode quality and reduced recombination under forward bias, which sharpened the J–V knee and increased curve squareness in Figure 6. The J_{SC} increased from 34.70 to 43.91 mA/cm^2 because reduced electron trapping allowed more generated carriers to survive collection. The improvement in QE shown in Figure 6 further supports the enhanced carrier collection at lower capture cross-sections.

3.5. Effect of series resistance

Series resistance is a key electrical loss parameter in solar cells. It arises from the finite conductivity of the transparent conducting material, absorber bulk, and contact interfaces. In CTL-free configurations, series resistance is particularly influential because selective transport layers are eliminated and carrier extraction depends strongly on ohmic pathways. The effect of series resistance was investigated by varying R_s from 0 to 5 Ω cm^2, as shown in Figure 7. The V_{OC} remained unchanged at 0.88 V across the full range because the net current is zero under open-circuit conditions and no voltage drop occurs across R_s. The J_{SC} showed only a marginal decrease from 43.91 to 43.86 mA/cm^2, indicating that photogeneration and carrier transport in the absorber were largely unaffected by moderate series resistance under short-circuit conditions.

In contrast, the FF decreased monotonically from 57.90% to 41.93% as series resistance increased. The PCE consequently decreased from 22.30% to 16.13%, primarily because of the FF loss. Minimizing series resistance is therefore essential for high-efficiency CTL-free PSCs. Practical strategies include optimizing FTO conductivity, improving the electrical quality of the La_2NiMnO_6 absorber through defect control, and ensuring low-resistance, well-matched back contacts. The overlapping QE curves in Figure 7 indicate that carrier collection remained largely unchanged, supporting the nearly constant J_{SC}. These trends are consistent with the diode model in Eq. (12) [41].

$$J = J_{ph} - J_0\left[\exp\left(\frac{q(V + JR_s)}{nkT}\right) - 1\right] - \frac{V + JR_s}{R_{sh}}, \tag{12}$$

where J_0 is the reverse current density, J is the output current density, J_{ph} is the photocurrent density, R_s is the series resistance, R_{sh} is the shunt resistance, T is temperature, V is the applied voltage, k is the Boltzmann constant, n is the ideality factor, and q is the elementary charge.

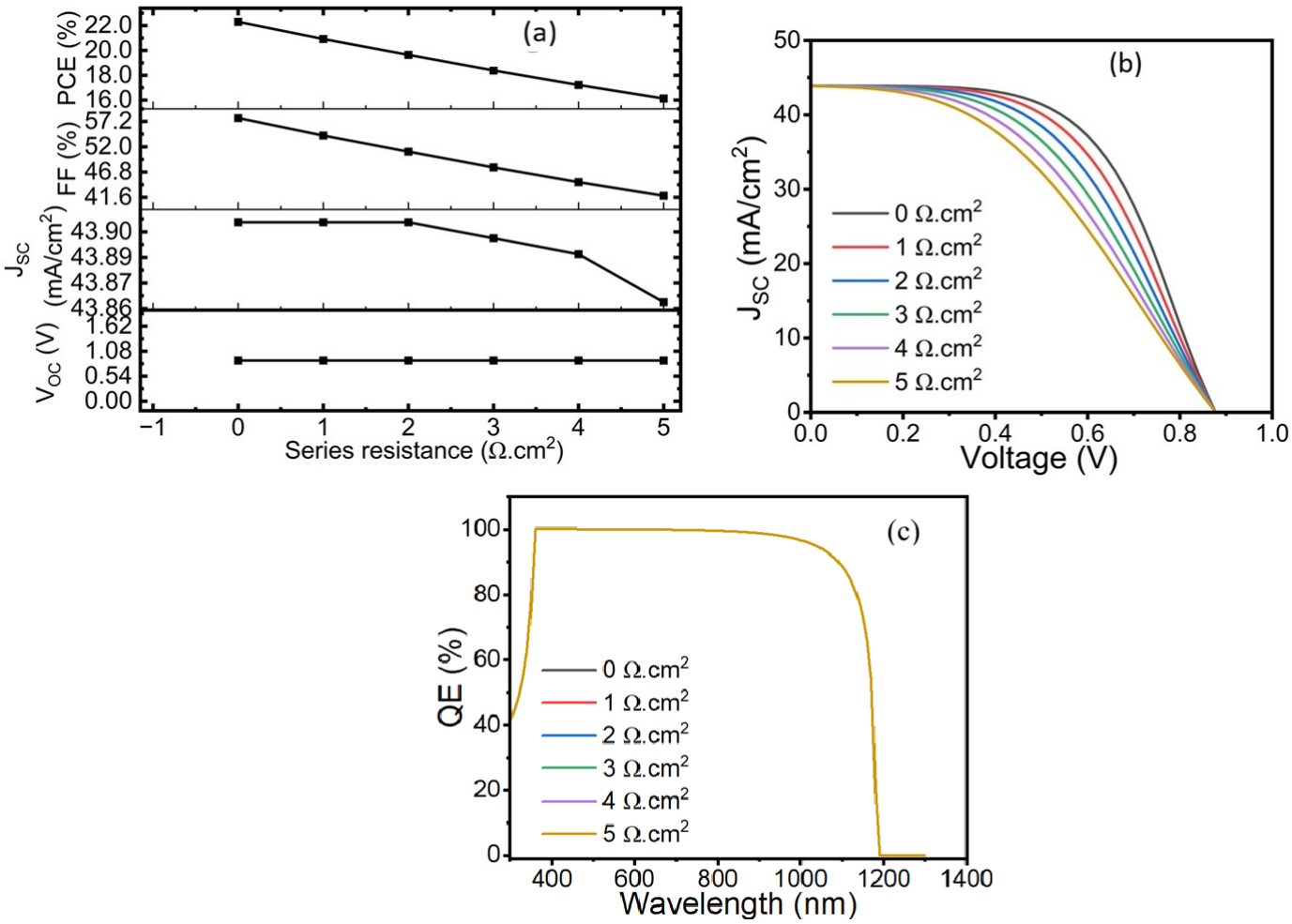

Figure 7: (a) Variation of V_{OC}, J_{SC}, FF, and PCE with series resistance, (b) associated J–V curves, and (c) QE plots.

3.6. Influence of shunt resistance

Shunt resistance represents parasitic leakage pathways that allow carriers to bypass the external circuit. Such pathways typically originate from bulk defects, pinholes, grain boundaries, or imperfect interfaces [54]. In CTL-free PSCs, where the absorber directly contacts the electrodes, shunt resistance is especially important. The effect of shunt resistance was analyzed by varying R_{sh} from 10^1 to $10^5\,\Omega\,cm^2$, as shown in Figure 8. The device exhibited a severely reduced V_{OC} of 0.43 V at $R_{sh} = 10^1\,\Omega\,cm^2$. This voltage loss resulted from substantial leakage currents that short-circuited photogenerated carriers and prevented sufficient quasi-Fermi-level splitting. As R_{sh} increased, leakage current was suppressed, and V_{OC} recovered sharply to 0.82 V at $10^2\,\Omega\,cm^2$ and saturated at 0.88 V for $10^4\,\Omega\,cm^2$.

The J_{SC} remained constant at 43.91 mA/cm^2 across the entire R_{sh} range because, under short-circuit conditions, carrier extraction is governed mainly by photogeneration and the built-in electric field rather than by leakage pathways. The FF increased from 25.58% to 57.89% as shunt resistance increased. Low R_{sh} distorts the J–V characteristics near the maximum power point by creating additional current losses under forward bias. Increasing R_{sh} reduces leakage, restores diode rectification, and improves curve squareness. The PCE increased from 4.81% at the lowest R_{sh} to 22.30%, showing that high shunt resistance is required for efficient CTL-free PSCs. The shunt current can be described by Eq. (13) [41].

$$J_{sh} = \frac{V + JR_s}{R_{sh}}, \tag{13}$$

where J_{sh} is the shunt current density. The overlapping QE curves in Figure 8 further indicate that carrier collection remained nearly unchanged across the range of shunt resistance.

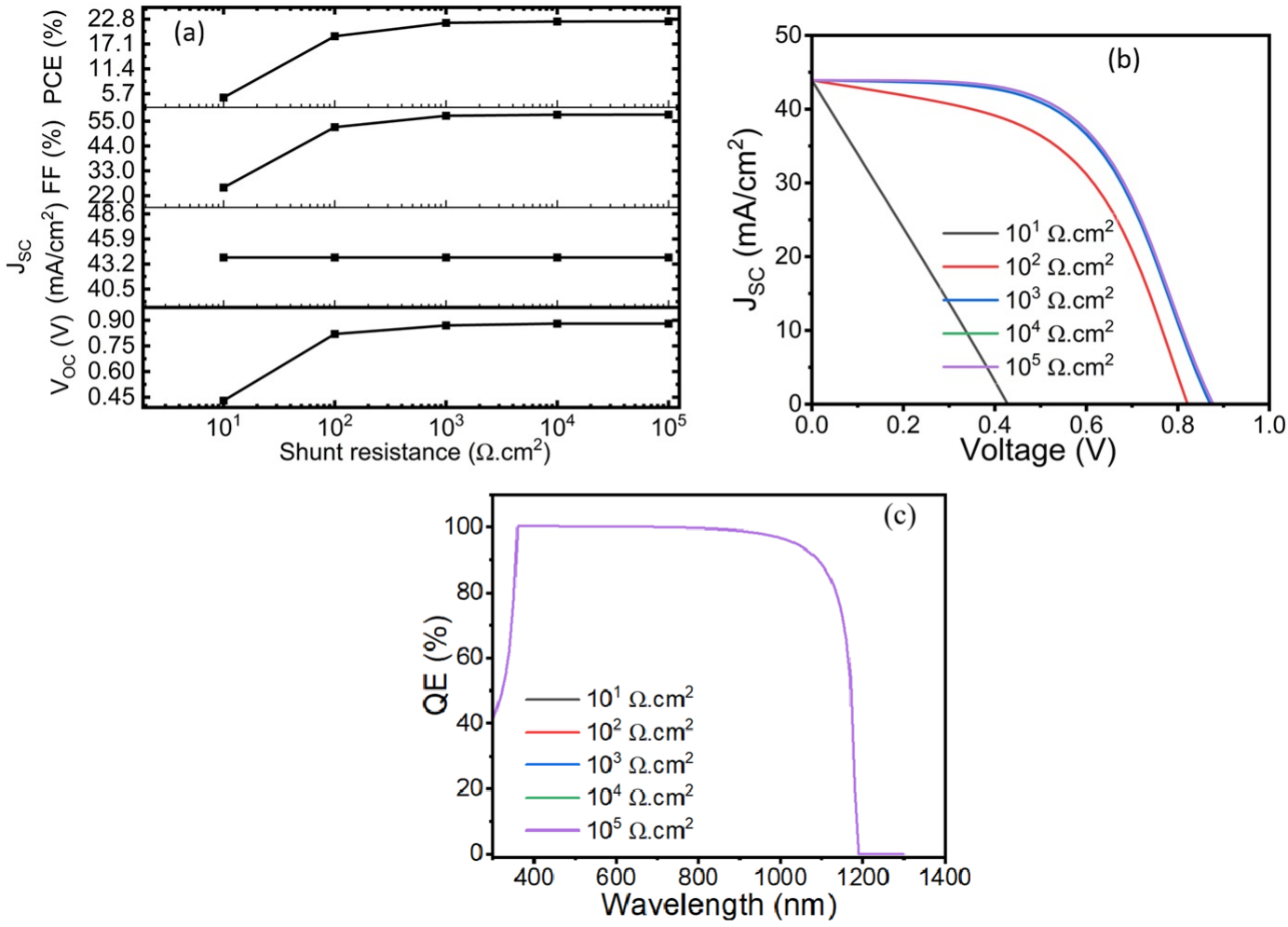

Figure 8: (a) Variation of V_{OC}, J_{SC}, FF, and PCE with shunt resistance, (b) associated J–V curves, and (c) QE plots.

Table 6: Error margins and sensitivity of thickness, bulk defect density, and electron capture cross-section.

Parameter varied	Range tested	PCE_{max} (%)	PCE_{min} (%)	ΔPCE (%)	Error margin (%)	Sensitivity	Class
Thickness (μm)	0.4–0.9	23.27	21.94	1.33	5.715	0.057	Low
Defect density (cm^{-3})	10^{16}–10^{20}	30.55	5.43	25.12	82.226	0.822	High
ECCS (cm^2)	10^{-15}–10^{-19}	22.30	3.08	19.22	86.188	0.862	High

Note: ECCS denotes electron capture cross-section in the absorber.

3.7. Error margins and sensitivity

Error-margin and sensitivity analyses are important for evaluating how variations in design parameters, such as film thickness, defect density, and electron capture cross-section, affect device performance. Identifying the parameters that most strongly influence PCE helps guide material-quality improvement, fabrication control, and reliability under realistic manufacturing conditions [55]. The error margins and sensitivity were calculated using Eqs. (14) and (15) [56]; the results are presented in Table 6 [57].

$$\text{Error margin} = \left(\frac{PCE_{max} - PCE_{min}}{PCE_{max}}\right) \times 100, \tag{14}$$

$$\text{Sensitivity} = \frac{\text{Error margin}}{100}. \tag{15}$$

Table 6 shows that photovoltaic performance is not equally affected by all material parameters. Thickness variation showed the lowest sensitivity and error margin, indicating that the PCE is relatively stable against absorber-thickness variation within the

Table 7: Comparison of performance metrics between experimental and simulated La_2NiMnO_6-based perovskite solar cells.

Perovskite solar cell	Nature of carrier transport	Preparation method	PCE (%), FF (%), J_{SC} (mA/cm^2), V_{OC} (V)	Reference
FTO/La_2NiMnO_6/Au	CTL-free	SCAPS-1D	30.58, 73.04, 40.79, 1.03	This work
FTO/La_2NiMnO_6/C	CTL-free	SCAPS-1D	30.34, 74.18, 40.79, 1.00	This work
FTO/$MAPbI_3$/carbon	CTL-free	SCAPS-1D	12.01, not available	[6]
FTO/$MAPbI_3$/Au	CTL-free	SCAPS-1D	12.35, 82.67, 17.53, 0.852	[10]
PET/IZO/SnO_2/$Cs_{0.17}FA_{0.83}PbI_{0.7}Br_{0.3}$/Au	HTL-free	Experiment	22.3	[59]
ITO/WS_2/La_2NiMnO_6/CFTS/Se	CTL-based	SCAPS-1D	20.18	[22]
FTO/TiO_2/La_2NiMnO_6/NiO/carbon	CTL-based	Experiment	4.5	[20]
FTO/SnO_2/La_2NiMnO_6/MoO_3/Au	CTL-based	SCAPS-1D	29.20, 87.14, 27.18, 1.23	[23]
FTO/ZnO/La_2NiMnO_6/Cu_2O/Au	CTL-based	SCAPS-1D	25.44, 82.69, 27.89, 1.11	[24]
TCO/TiO_2/Cs_2TiBr_6/La_2NiMnO_6/Cu_2O/Au	CTL-based	SCAPS-1D	33.71, 83.85, 43.83, 0.9171	[21]
ITO/TiO_2/La_2NiMnO_6/Spiro-OMeTAD	CTL-based	SCAPS-1D	22.0, not available	[25]

investigated range. This suggests that small deviations in film thickness during fabrication are unlikely to cause major PCE losses. In contrast, defect density showed high sensitivity and a large error margin, confirming that recombination through defect states strongly limits device performance. Electron capture cross-section exhibited the highest sensitivity, indicating that the recombination activity of defect states depends not only on the number of defects but also on how effectively those defects capture photogenerated carriers. Therefore, reducing trap density and capture activity is critical for high-performance La_2NiMnO_6-based CTL-free PSCs.

3.8. Photovoltaic performance of the optimized PSC

The optimized FTO/La_2NiMnO_6/Au PSC was prepared by reducing absorber thickness to 0.4 μm, minimizing bulk defect density to 10^{16} cm^{-3}, and setting series and shunt resistances to 0 and $10^5\,\Omega\,$cm^2, respectively. Compared with the prototype, the optimized cell exhibited significantly improved photovoltaic performance. The V_{OC} increased from 0.88 to 1.03 V, the FF increased to 73.04%, and the PCE increased to 30.58%, while J_{SC} decreased slightly to 40.79 mA/cm^2, as shown in Figure 9. The increases in V_{OC} and FF are attributed to suppressed trap-assisted recombination caused by reduced bulk defect density, which improves carrier lifetime, charge transport, and extraction efficiency. Although the thinner absorber slightly reduced J_{SC} through reduced photon absorption, this loss was outweighed by lower recombination losses and improved electrical quality.

The optimized PCE of 30.58% approaches the theoretical efficiency range predicted for absorbers with band gaps near 1.05 eV [58]. However, the simulated V_{OC} is obtained under idealized assumptions and should be interpreted as an upper-bound numerical result rather than a direct representation of experimentally attainable output. The lower QE of the optimized device compared with the prototype supports the reduced J_{SC} associated with the thinner absorber layer.

Figure 9 also shows the carrier generation and recombination profiles for the optimized FTO/La_2NiMnO_6/Au device. The carrier generation rate is strongly localized within the absorber and reaches a peak of approximately 2.21×10^{22} cm^{-3}s^{-1} near the front of the absorber. It then decreases gradually toward the back of the device. The high generation rate supports the large J_{SC} of the optimized cell. The recombination rate shows a pronounced peak of about 3.79×10^{20} cm^{-3}s^{-1} within the FTO region and remains low through most of the absorber thickness, supporting efficient charge collection in the optimized structure.

Table 7 compares the present results with related absorber-based works in the literature. The FTO/La_2NiMnO_6/Au device achieved a PCE of 30.58%, which exceeds the highest reported PCE of 29.20% for a single-absorber La_2NiMnO_6-based PSC, FTO/SnO_2/La_2NiMnO_6/MoO_3/Au, in Ref. [23]. This improvement is attributed to proper band alignment between the absorber and contacts, the ambipolar capacity of the absorber to separate and transport carriers without CTLs, and the absence of additional interface defects from CTLs. Cheragee *et al.* [21] reported a higher PCE of 33.71% using a double absorber architecture, TCO/TiO_2/Cs_2TiBr_6/La_2NiMnO_6/Cu_2O/Au. However, such multilayer structures may increase fabrication cost and introduce additional defect and series-resistance channels. The performance of the present device indicates that CTL-free designs can offer an economically viable path toward high-performance La_2NiMnO_6-based PSCs.

3.9. Impact of temperature on the optimized PSC

Studying temperature dependence is essential for understanding thermally induced changes in carrier dynamics, recombination mechanisms, and device stability under realistic operating conditions [41, 50, 60]. The optimized FTO/La_2NiMnO_6/Au PSC maintained stable performance over 280–330 K, as shown in Figure 10. Increasing temperature caused a slight decrease in V_{OC}, from 1.04 to 1.02 V, while J_{SC} remained constant at 40.79 mA/cm^2. In contrast, the FF increased from 69.94% to 75.73%, leading to a gradual PCE increase from 29.54% to 31.51%. These results indicate good thermal tolerance and even a benefit from moderate temperature increase within the investigated range.

The slight V_{OC} decline with increasing temperature is expected and is associated with enhanced thermal excitation and recombination. As temperature increases, the effective band gap narrows and intrinsic carrier concentration increases, reducing the built-in

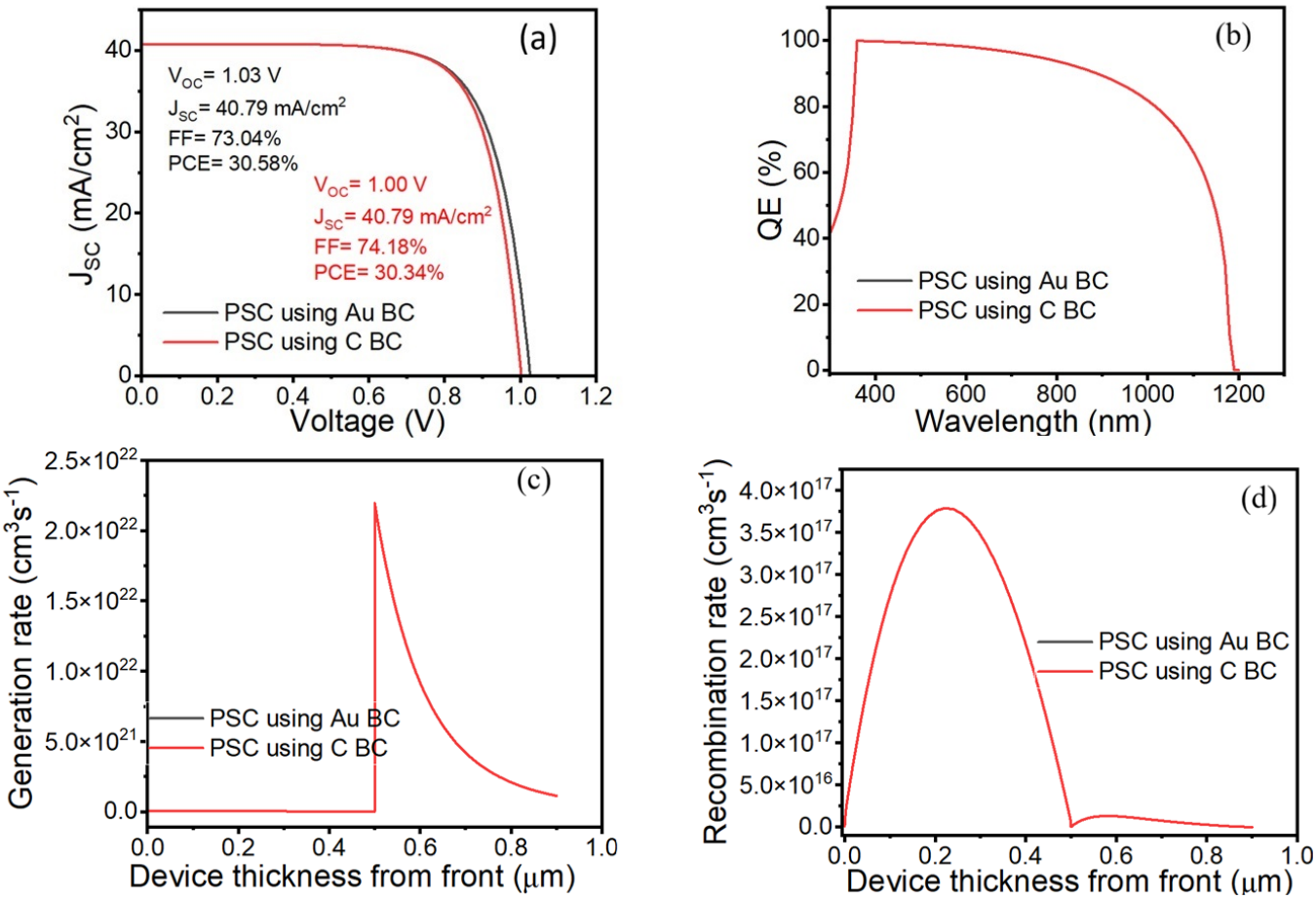

Figure 9: (a) J–V curves of optimized La_2NiMnO_6-based CTL-free PSCs using Au and C back contacts, (b) QE plots, (c) carrier generation rate, and (d) carrier recombination rate. BC denotes back contact, and C denotes carbon back contact.

potential and lowering V_{OC}. The relationship among these quantities is expressed in Eq. (16) [61].

$$\frac{dV_{OC}}{dT} = \frac{V_{OC} - E_g/e}{T} = \frac{1}{e}\frac{dE_g}{dT}, \tag{16}$$

where T is temperature, E_g is band-gap energy, and e is the electronic charge. The steady J_{SC} indicates that photocurrent generation and carrier collection remain essentially unaffected by temperature variation. The increase in FF suggests that higher temperature may improve carrier mobility, reduce transport barriers, or enhance charge extraction at the Au back contact. This FF increase compensates for the slight V_{OC} loss, producing a net PCE improvement.

3.10. Influence of sun concentration on the optimized PSC

The influence of sun concentration, or illumination intensity, was explored to understand light-intensity-dependent carrier generation, recombination, and charge transport, and to evaluate suitability for concentrator photovoltaic applications [61–63]. As illumination intensity increased from 1 sun (100 mW/cm^2) to 50 suns (5000 mW/cm^2), the PCE increased from 30.34% to 39.21%, indicating strong responsiveness to concentrated light, as shown in Figure 11. The J_{SC} increased linearly from 40.79 to 2356.08 mA/cm^2 because higher photon flux generated more charge carriers. This linearity confirms that the absorber maintained efficient photogeneration and carrier collection under high illumination.

The V_{OC} also increased from 1.00 to 1.13 V, consistent with the logarithmic dependence of V_{OC} on light intensity. As carrier concentration increased under higher illumination, quasi-Fermi-level splitting became larger, improving V_{OC}. The FF remained relatively stable, decreasing only slightly from 74.18% to 73.71%, which may be attributed to increased recombination, resistive effects, or heating under high illumination. Nevertheless, the small change indicates that the device maintains good charge transport and extraction efficiency under elevated light intensity.

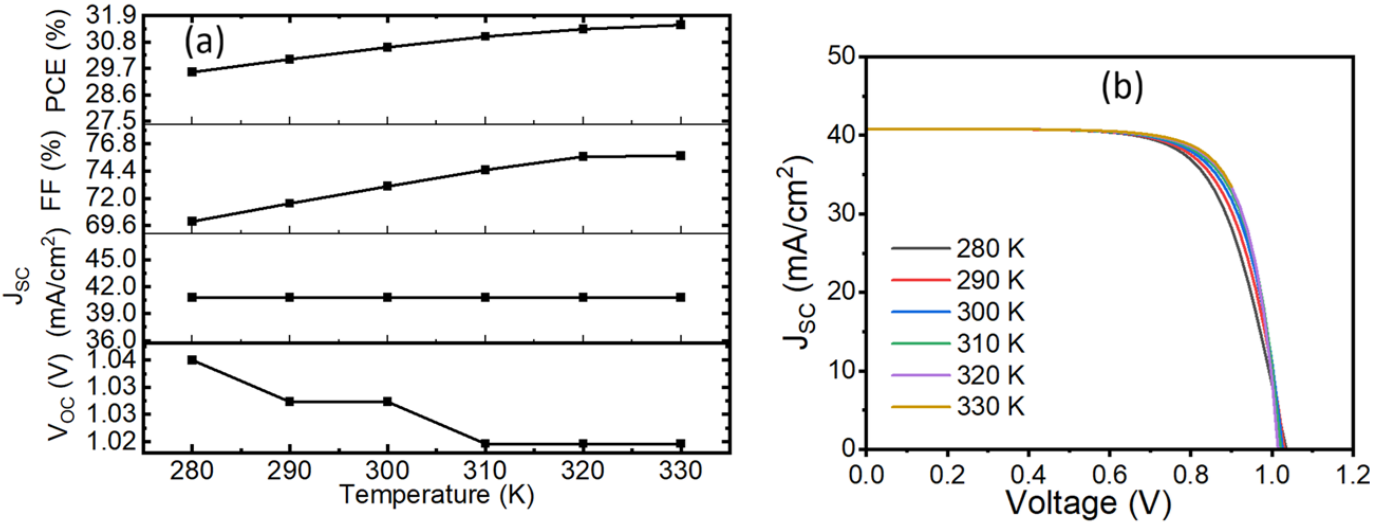

Figure 10: (a) Variation of V_{OC}, J_{SC}, FF, and PCE with temperature and (b) associated J–V curves.

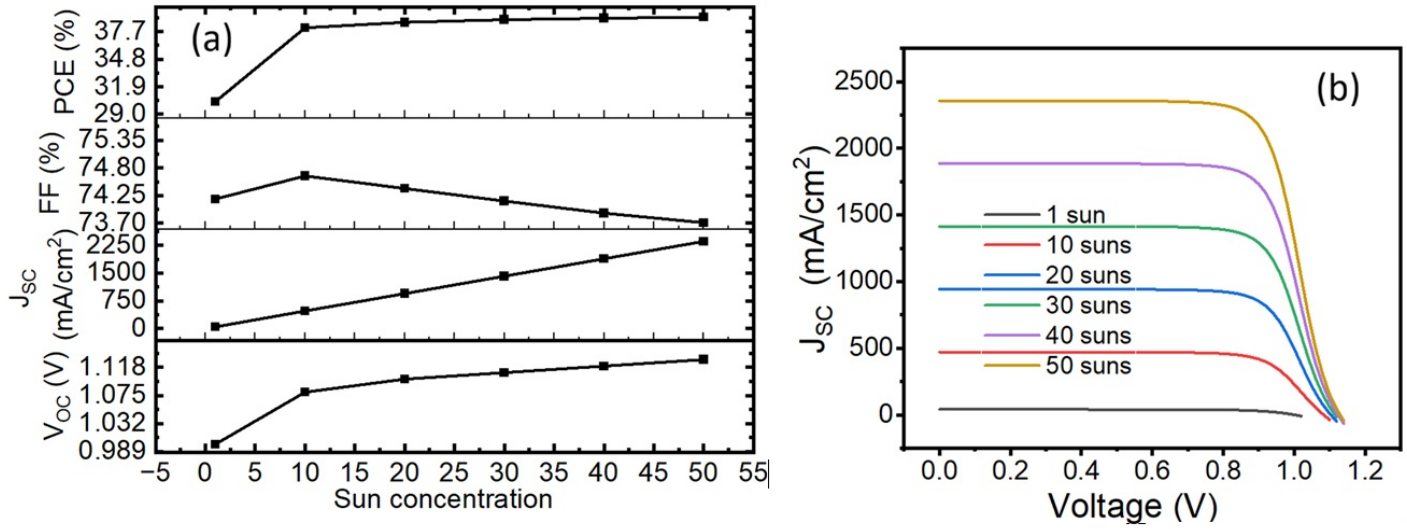

Figure 11: (a) Dependence of V_{OC}, J_{SC}, FF, and PCE on sun concentration or illumination intensity and (b) associated J–V curves.

3.11. Simulations using the cost-effective carbon back contact

Carbon back contacts provide a practical route toward stable and economically viable PSCs. Compared with conventional Au back electrodes, carbon materials are more abundant and substantially less expensive. Carbon also offers stable performance, simple processing, and compatibility with scalable fabrication. Recent studies show that carbon-electrode PSCs can exhibit enhanced ambient and operational stability, making carbon a promising replacement for costly metal contacts in durable, large-scale PSCs [64–66]. The work function of carbon (5.0 eV) is close to that of Au (5.1 eV), enabling good energy alignment with the La_2NiMnO_6 absorber.

The optimized FTO/La_2NiMnO_6/C PSC showed a PCE of 30.34%, which is highly comparable to the 30.58% PCE of the optimized FTO/La_2NiMnO_6/Au device, as shown in Figure 9. Compared with the Au-contact device, the carbon-contact cell showed a slightly lower V_{OC} of 1.00 V, while J_{SC} remained unchanged at 40.79 mA/cm^2. The FF increased from 73.04% for the Au-contact cell to 74.18% for the carbon-contact cell. As a result, PCE decreased by only 0.24 percentage points, indicating that replacing Au with carbon does not substantially compromise photovoltaic performance.

The lower V_{OC} in the carbon-based device can be related to the difference in work function between Au and carbon. Gold generally offers slightly more favorable band alignment and hole extraction at the back contact, which can maintain a higher built-in potential and reduce interfacial recombination. Conversely, carbon introduces a slightly less ideal contact, producing the observed small V_{OC} decrease. Nevertheless, the carbon back contact yielded a higher FF, suggesting improved charge collection and possibly

lower series resistance or more favorable interfacial charge transfer. The unchanged J_{SC} shows that replacing Au with carbon does not affect light harvesting or carrier generation in the optimized PSC.

4. Conclusion

This work demonstrated the feasibility of high-performance, cost-effective CTL-free PSCs based on La_2NiMnO_6 using SCAPS-1D simulations. The proposed FTO/La_2NiMnO_6/Au configuration recorded an optimized PCE of 30.58%, outperforming many reported La_2NiMnO_6-based PSCs while operating under realistic material conditions. The results show that absorber properties, specifically defect density and electron capture cross-section, govern device performance, whereas thickness has lower sensitivity, indicating favorable fabrication tolerance. The CTL-free architecture minimizes interface-related recombination pathways, enabling efficient ambipolar charge transport and a simplified device structure. Replacing Au with carbon produced a comparable PCE of 30.34% for the FTO/La_2NiMnO_6/C design, highlighting strong potential for low-cost and scalable fabrication. The solar cell also showed excellent thermal stability over 280–330 K and enhanced performance under concentrated illumination from 1 to 50 suns. This study establishes La_2NiMnO_6 as a promising absorber for next-generation simplified PSCs and provides design guidance for practically realizable, stable, and economically viable CTL-free photovoltaic technologies.

Data availability

All the data used in this work are contained in the manuscript. There are no additional data related to this work to share.

Declaration of competing interest

The authors declare that there are no financial interests, commercial affiliations, or other potential conflicts of interest that could have influenced the objectivity of this research or the writing of this paper.

Funding

This work was supported by the UKRI Ayrton Fund: REACH-PSM – Resilient Renewable Energy Access through Community-Driven Holistic Development in Perovskite Solar Module Manufacturing.

References

[1] M. A. Green, E. D. Dunlop, J. Hohl-Ebinger, M. Yoshita, N. Kopidakis, X. Hao & A. W. Y. Ho-Baillie, “Solar cell efficiency tables (Version 66)”, Progress in Photovoltaics: Research & Applications **33** (2025) 795. https://onlinelibrary.wiley.com/doi/10.1002/pip.3919.

[2] National Renewable Energy Laboratory (NREL), “Best research-cell efficiency chart”, Golden, CO, USA, 2025. Available online: https://www.nrel.gov/pv/cell-efficiency.html.

[3] K. Wang, J. Zheng, R. Yu & Z. Tan, “Recent progress on high efficiency perovskite/organic tandem solar cells”, Nanomaterials **15** (2025) 745. https://doi.org/10.3390/nano15100745.

[4] M. Afroz, R. K. Ratnesh, S. Srivastava & J. Singh, “Perovskite solar cells: progress, challenges, and future avenues to clean energy”, Solar Energy **287** (2025) 113205. https://doi.org/10.1016/j.solener.2024.113205.

[5] J. Han, K. Park, S. Tan, N. Li, D. H. Kim, N.-G. Park, M. Grätzel & M. K. Nazeeruddin, “Perovskite solar cells”, Nature Reviews Methods Primers **5** (2025) 3. https://doi.org/10.1038/s43586-024-00373-9.

[6] T. Ye, Y. Hou, A. Nozariasbmarz, D. Yang, J. Yoon, L. Zheng, K. Wang, K. Wang, S. Ramakrishna & S. Priya, “Cost-effective high-performance charge-carrier-transport-layer-free perovskite solar cells achieved by suppressing ion migration”, ACS Energy Letters **6** (2021) 3044. https://doi.org/10.1021/acsenergylett.1c01186.

[7] J.-F. Liao, W.-Q. Wu, Y. Jiang, J. Zhong, L. Wang & D.-B. Kuang, “Understanding of carrier dynamics, heterojunction merits and device physics: towards designing efficient carrier transport layer-free perovskite solar cells”, Chemical Society Reviews **49** (2020) 354. https://doi.org/10.1039/c8cs01012a.

[8] K. Choodam, N. Kamjam, N. Sukpan, C. Seriwattanachai, A. Inna, K. K. S. Thant, L. Srathongsian, R. Supruangnet, H. Nakajima, A. Kaewprajak, P. Kumnorkaew, D. Wongratanaphisan, P. Ruankham, P. Pakawatpanurut & P. Kanjanaboos, “Economical perovskite solar cell enabled by triple cost-reduction strategies”, Small Science **6** (2026) e202500451. https://doi.org/10.1002/smsc.202500451.

[9] L. Wang, S. Yang, Q. Han, F. Yu, H. Zhang, X. Cai, C. Zhang, L. Gao & T. Ma, “Carrier transport layer-free perovskite solar cells”, ChemSusChem **14** (2021) 4776. https://doi.org/10.1002/cssc.202101592.

[10] S. Bhattarai, A. Sharma, D. Muchahary, M. Gogoi & T. D. Das, “Carrier transport layer free perovskite solar cell for enhancing the efficiency: a simulation study”, Optik **243** (2021) 167492. https://doi.org/10.1016/j.ijleo.2021.167492.

[11] Y. Liu, Z. Zhang, T. Wu, Y. Li, H. Wang, X. Chen, J. Zhao, H. Li, L. Zhang & Y. Chen, “Cost effectivities analysis of perovskite solar cells: will it outperform crystalline silicon ones?”, Nano-Micro Letters **17** (2025) 219. https://doi.org/10.1007/s40820-025-01744-x.

[12] L. Etgar, P. Gao, Z. Xue, Q. Peng, A. K. Chandiran, B. Liu, M. K. Nazeeruddin & M. Grätzel, “Mesoscopic $CH_3NH_3PbI_3/TiO_2$ heterojunction solar cells”, Journal of the American Chemical Society **134** (2012) 17396. https://doi.org/10.1021/ja307789s.

[13] L. Huang, X. Sun, C. Li, R. Xu, J. Xu, Y. Du, Y. Wu, J. Ni, H. Cai, J. Li, Z. Hu & J. Zhang, “Electron transport layer-free planar perovskite solar cells: further performance enhancement perspective from device simulation”, Solar Energy Materials and Solar Cells **157** (2016) 1038. https://doi.org/10.1016/j.solmat.2016.08.025.

[14] W. Hui, X. Kang, B. Wang, D. Li, Z. Su, Y. Bao, L. Gu, B. Zhang, X. Gao, L. Song & W. Huang, “Stable electron-transport-layer-free perovskite solar cells with over 22% power conversion efficiency”, Nano Letters **23** (2023) 2195. https://doi.org/10.1021/acs.nanolett.2c04720.

[15] C. Huang, P. Lin, N. Fu, C. Liu, B. Xu, K. Sun, D. Wang, X. Zeng & S. Ke, "Facile fabrication of highly efficient ETL-free perovskite solar cells with 20% efficiency by defect passivation and interface engineering", Chemical Communications **55** (2019) 2777. https://doi.org/10.1039/C9CC00312F.

[16] P. R. Jubu, Z. S. Mbalaha, E. V. Tikyaa, O. S. Obaseki, K. O. Ighodalo, O. Adedokun, A. Nathan-Abutu, M. B. Ochang, Y. Yusof & M. Z. Pakhuruddin, "High-efficiency hole transport layer-free perovskite solar cells utilizing TiO_2, ZnO and bilayer TiO_2/ZnO electron transport layers: a simulation approach", Next Materials **9** (2025) 1. https://doi.org/10.1016/j.nxmate.2025.101166.

[17] A. Shpatz Dayan & L. Etgar, "Study of electron transport layer-free and hole transport layer-free inverted perovskite solar cells", Solar RRL **6** (2021) 2100578. https://doi.org/10.1002/solr.202100578.

[18] X. Yang, Q. Li, Y. Zheng, D. Luo, Y. Zhang, Y. Tu, L. Zhao, Y. Wang, F. Xu, Q. Gong & R. Zhu, "Perovskite hetero-bilayer for efficient charge-transport-layer-free solar cells", Joule **6** (2022) 1277. https://doi.org/10.1016/j.joule.2022.04.012.

[19] K. Yi, Q. Tang, Z. Wu & X. Zhu, "Unraveling the structural, dielectric, magnetic, and optical characteristics of nanostructured La_2NiMnO_6 double perovskites", Nanomaterials **12** (2022) 979. https://doi.org/10.3390/nano12060979.

[20] T. Sangavi, S. Vasanth, C. Viswanathan & N. Ponpandian, "Synergizing experimental and theoretical insights: unveiling the solar potential of La_2NiMnO_6 double perovskite for enhanced efficiency and sustainability in photovoltaics", Chemical Engineering Journal **486** (2024) 150216. https://doi.org/10.1016/j.cej.2024.150216.

[21] S. H. Cheragee, J. A. Akhi, M. Dev, M. M. Haque, M. A. Kabir, T. Hossain, M. T. Alam & M. J. Alam, "Optimized non-toxic double absorber perovskite solar cell with efficiency beyond 33%", Results in Optics **19** (2025) 100813. https://doi.org/10.1016/j.rio.2025.100813.

[22] M. K. Hossain, A. A. Arnab, G. F. I. Toki, I. Alam, M. H. K. Rubel, M. F. Rahman & H. Bencherif, "Design insights into La_2NiMnO_6-based perovskite solar cells employing different charge transport layers: DFT and SCAPS-1D frameworks", Energy & Fuels **37** (2023) 13377. https://doi.org/10.1021/acs.energyfuels.3c02361.

[23] K. Ul Sahar, U. U. Rehman, E. Hussain, M. S. Javed, M. Ahmad, M. I. Khan, Y. Alqahtani & F. A. Alharthi, "Unraveling the potential of La_2NiMnO_6-based perovskite solar cells via SCAPS-1D simulations: insights into performance and charge dynamics", Journal of Electronic Materials **54** (2025) 6118. https://doi.org/10.1007/s11664-025-12041-z.

[24] A. Singh, V. Srivastava & S. Agarwal, "Enhancing the performance of lead-free La_2NiMnO_6 double perovskite solar cells through SCAPS-1D optimization", Journal of Optics **53** (2024) 3695. https://doi.org/10.1007/s12596-023-01527-w.

[25] D. Pal & S. Das, "Defect and interface engineering of highly efficient La_2NiMnO_6 planar perovskite solar cell: a theoretical study", Optical Materials **108** (2020) 110453. https://doi.org/10.1016/j.optmat.2020.110453.

[26] K. Boughanbour, M. Sahal, E. Oublal, N. Kumar, Y. Belkassmi & A. Kotri, "Simulation and optimization of $MAPbI_3$/$MASnI_3$ heterojunction perovskite solar cell with double ETL by SCAPS-1D software", Optical and Quantum Electronics **57** (2025) 1. https://doi.org/10.1007/s11082-025-08138-8.

[27] P. R. Jubu, F. K. Yam & K. T. Low, "Feasibility study on synthesis of gallium oxide nanostructures on glass substrate by chemical vapor deposition", Thin Solid Films **710** (2020) 138257. https://doi.org/10.1016/j.tsf.2020.138257.

[28] E. Danladi, W. Mutah, P. R. Jubu, K. A. Ogunmoye, Z. L. Abubakar, D. A. Bala, N. N. Tasiu, A. Idris, F. Aungwa, M. I. Amanyi, E. Akpogumah, N. I. Noah & F. Ezemaj, "Photovoltaic performance of $CsPbBr_3$-based perovskite solar cell with TiO_2 and quaternary chalcogenide Cu_2FeSnS_4 as charge transport channels: unlocking >26% efficiency via SCAPS-1D investigation", Next Energy **9** (2025) 1. https://doi.org/10.1016/j.nxener.2025.100423.

[29] A. Raj, A. Anshul, V. Tuli, P. K. Singh, R. C. Singh & M. Kumar, "Effect of appropriate ETL on quantum efficiency of double perovskite La_2NiMnO_6 based solar cell device via SCAPS simulation", Materials Today: Proceedings **47** (2021) 1656. https://doi.org/10.1016/j.matpr.2021.04.581.

[30] W. Lin, X. Chen, Z. Ji, W. Gao, N. Zhao, M. Li, D. Zhang, Y. Ling, J. Wu, K. Huang & J. Yu, "Optimization of Cs_2TiBr_6-based perovskite solar cells with double hole transport layer by SCAPS-1D simulation", Materials Today Communications **46** (2025) 112841. https://doi.org/10.1016/j.mtcomm.2025.112841.

[31] E. Danladi, L. F. Obagboye, S. Aisida, F. I. Ezema, O. Okorie, J. A. Bwamba, P. A. Emmanuel, A. A. Hussaini, P. R. Jubu & A. C. Ozurumba, "20.730% highly efficient lead-free $CsSnI_3$-based perovskite solar cells with various charge transport materials: a SCAPS-1D study", Multiscale and Multidisciplinary Modeling, Experiments and Design **8** (2025) 114. https://doi.org/10.1007/s41939-024-00701-2.

[32] M. V. Kavithaa, C. K. Anjalia & K. S. Sudheer, "Device simulation and optimization of HTL-free perovskite solar cell with $CH_3NH_3SnBr_3$ as the absorber layer using SCAPS-1D", Journal of Ovonic Research **20** (2024) 245. https://doi.org/10.15251/JOR.2024.202.245.

[33] G. Vishnupriya & P. Sathya, "Computational study of a novel combination of dual-absorber structured perovskite solar cell with theoretical efficiency of 36.37%", Frontiers in Energy Research **13** (2025) 1631201. https://doi.org/10.3389/fenrg.2025.1631201.

[34] M. H. Rahman, F. Rayhan, O. Ghosh, A. E. Bajwa, M. S. Hosen, M. S. Uddin, A. M. Al Mashud, A. Kumer & M. M. H. Bappy, "An in-depth analysis of $CsSnCl_3$-based perovskite solar cell with diverse ETLs and $C_6TBTAPH_2$ as HTL: a numerical analysis", Journal of Inorganic and Organometallic Polymers and Materials **35** (2025) 7762. https://doi.org/10.1007/s10904-024-03452-2.

[35] M. Shirazi, "Optimizing key parameters to enhance the performance of lead-free perovskite solar cells with a $Cs_2AgBiCl_6$ absorber layer using SCAPS-1D simulation", Journal of Optics **54** (2025) 234. https://doi.org/10.1007/s12596-025-02557-2.

[36] S. M. Alghamdi, "High-efficiency $BaZrSe_3$/ZnSe heterojunction solar cells: a numerical simulation approach for next-generation photovoltaics", Results in Engineering **28** (2025) 107195. https://doi.org/10.1016/j.rineng.2025.107195.

[37] N. Chawki, M. Rouchdi, M. Alla & B. Fares, "Simulation & analysis of high-performance hole transport material $SrZrS_3$-based perovskite solar cells with a theoretical efficiency approaching 26%", Solar Energy **262** (2023) 111913. https://doi.org/10.1016/j.solener.2023.111913.

[38] A. Bar, S. K. Saha, K. Ghorui, B. Tudu & S. Sarkar, "Numerical design & performance optimization of emerging $SrZrS_3$-based solar cells integrated with ZrS_2 & CZTS transport layers", SSRN Electronic Journal (2025). https://doi.org/10.2139/ssrn.5500356.

[39] P. K. Patel, "Device simulation of highly efficient eco-friendly $CH_3NH_3SnI_3$ perovskite solar cell", Scientific Reports **11** (2021) 3082. https://doi.org/10.1038/s41598-021-82817-w.

[40] M. Wang, Y. Yin, W. Cai, J. Liu, Y. Han, Y. Feng, Q. Dong, Y. Wang, J. Bian & Y. Shi, "Synergetic co-modulation of crystallization and co-passivation of defects for $FAPbI_3$ perovskite solar cells", Advanced Functional Materials **32** (2022) 2108567. https://doi.org/10.1002/adfm.202108567.

[41] E. Danladi, E. E. Oguzie & F. I. Ezema, "Highly efficient 25.562% $Cs_2AgBiBr_6$ double perovskite solar cell with copper barium tin sulfide and ZnO as charge transport channels: an intuition from a theoretical study using SCAPS-1D", Journal of Photonics for Energy **15** (2025) 024501. https://doi.org/10.1117/1.JPE.15.024501.

[42] S. M. Sze & K. K. Ng, *Physics of Semiconductor Devices*, 3rd ed., John Wiley & Sons, Hoboken, NJ, USA, 2007, p. 42. Available online: https://www.wiley.com/en-us/shop/general-introductory-electrical-electronics-engineering/physics-of-semiconductor-devices-3rd-edition-p-9780470068328.

[43] G. E. Eperon, T. Leijtens, K. A. Bush, R. Prasanna, T. Green, J. T.-W. Wang, D. P. McMeekin, G. Volonakis, R. L. Milot, R. May, A. Palmstrom, D. J. Slotcavage, R. A. Belisle, J. B. Patel, E. S. Parrott, R. J. Sutton, W. Ma, F. Moghadam, B. Conings & M. D. McGehee, "Perovskite-perovskite tandem photovoltaics with optimized band gaps", Science **354** (2016) 861. https://doi.org/10.1126/science.aaf9717.

[44] D. Zhao, Y. Yu, C. Wang, W. Liao, N. Shrestha, C. R. Grice, A. J. Cimaroli, L. Guan, R. J. Ellingson, K. Zhu, R. G. Xiong & Y. Yan, "Low-bandgap mixed tin–lead iodide perovskite absorbers with long carrier lifetimes for all-perovskite tandem solar cells", Nature Energy **2** (2017) 17018. https://doi.org/10.1038/nenergy.2017.18.

[45] U. U. Rehman, R. S. Almufarij, K. U. Sahar, A. Ashfaq, M. M. Saad, E. Alsubhe, O. Albeydani, S. M. Alghamdi, K. Mahmood & C. M. Wang, "Efficiency improvement of lead-free La_2NiMnO_6-based double perovskite solar cells using numerical simulation", Energy Technology **12** (2024) 2301165. https://doi.org/

10.1002/ente.202301165.
[46] P. Singh & N. M. Ravindra, "Temperature dependence of solar cell performance–an analysis", Solar Energy Materials and Solar Cells **101** (2012) 36. https://doi.org/10.1016/j.solmat.2012.02.019.
[47] A. H. M. Smets, K. Jäger, O. Isabella, R. A. C. M. M. van Swaaij & M. Zeman, *Solar Energy: The Physics & Engineering of Photovoltaic Conversion, Technologies & Systems*, Delft University of Technology, Delft, Netherlands, 2016, p. 34. Available online: https://www.researchgate.net/publication/304658624_Solar_Energy_-_The_physics_and_engineering_of_photovoltaic_conversion_technologies_and_systems.
[48] P. R. Jubu, S. K. Omotayo, E. E. Oguzie, T. Imbur & M. Z. Pakhuruddin, "High-efficiency HTL-free i-n versus p-i-n InGaN single junction solar cells: a SCAPS-1D optimization study", Next Energy **11** (2026) 100540. https://doi.org/10.1016/j.nxener.2026.100540.
[49] J. Tao, C. Zhao, Z. Wang, Y. Chen, L. Zang, G. Yang, Y. Bai & J. Chu, "Suppressing non-radiative recombination for efficient and stable perovskite solar cells", Energy & Environmental Science **18** (2025) 509. https://doi.org/10.1039/D4EE02917H.
[50] P. R. Jubu, M. K. Omar, S. K. Omotayo & M. Z. Pakhuruddin, "Numerical simulation on electrical characteristics of high efficiency PPN homojunction InGaN photovoltaic solar cell", Next Materials **11** (2026) 101597. https://doi.org/10.1016/j.nxmate.2026.101597.
[51] K. V. Seshaiah & J. H. Kim, "Nature of defects and their passivation engineering for advancements in perovskite solar cells", Chemical Engineering Journal **492** (2024) 152370. https://doi.org/10.1016/j.cej.2024.152370.
[52] Y. Wang, Y. Cheng, C. Yin, J. Zhang, J. You, J. Wang, J. Wang & J. Zhang, "Manipulating crystal growth and secondary phase PbI_2 to enable efficient and stable perovskite solar cells with natural additives", Nano-Micro Letters **16** (2024) 183. https://doi.org/10.1007/s40820-024-01400-w.
[53] W. Shockley & W. T. Read, "Statistics of the recombinations of holes and electrons", Physical Review **87** (1952) 835. https://doi.org/10.1103/PhysRev.87.835.
[54] C. Liu, Z. Huang, X. Hu, X. Meng, X. Huang, L. Xiong, J. Tan & Y. Chen, "Grain boundary modification via F4TCNQ to reduce defects of perovskite solar cells with excellent device performance", ACS Applied Materials & Interfaces **10** (2018) 1909. https://doi.org/10.1021/acsami.7b15031.
[55] M. Kumar, S. Rani, X. Wang & V. N. Singh, "Unlocking the full potential of solar cell materials: parameter sensitivity analysis and optimization using response surface modeling", Materials Advances **6** (2025) 1. https://doi.org/10.1039/d4ma00728j.
[56] A. Q. Jakhrani, A. K. Othman, A. R. H. Rigit, S. R. Samo & S. A. Kamboh, "Sensitivity analysis of a standalone photovoltaic system model parameters", Journal of Applied Sciences **13** (2013) 220. https://doi.org/10.3923/jas.2013.220.231.
[57] P. R. Jubu, B. J. Akeredolu, S. J. Ikwee, K. O. Ighodalo, O. S. Obaseki, Z. S. Mbalah, S. K. Omotayo, Y. Yusof & M. Z. Pakhuruddin, "Performance optimization of perovskite solar cells using p-InGaN as a hole transport layer: a numerical comparison with spiro-OMeTAD and HTL-free designs", Next Energy **11** (2026) 100510. https://doi.org/10.1016/j.nxener.2025.100510.
[58] S. Rühle, "Tabulated values of the Shockley–Queisser limit for single junction solar cells", Solar Energy **130** (2016) 139. https://doi.org/10.1016/j.solener.2016.02.015.
[59] C. Teixeira, P. Spinelli, L. A. Castriotta, D. Müller, S. Öz, L. Andrade, A. Mendes, A. Di Carlo, U. Würfel, K. Wojciechowski & D. Forgács, "Charge extraction in flexible perovskite solar cell architectures for indoor applications–with up to 31% efficiency", Advanced Functional Materials **32** (2022) 1. https://doi.org/10.1002/adfm.202206761.
[60] Q. Zhou, B. Wang, R. Meng, J. Zhou, S. Xie, X. Zhang, J. Wang, S. Yue, B. Qin, H. Zhou & Y. Zhang, "Understanding temperature-dependent charge extraction and trapping in perovskite solar cells", Advanced Functional Materials **30** (2020) 2000550. https://doi.org/10.1002/adfm.202000550.
[61] V. M. Le Corre, T. S. Sherkar, M. Koopmans & L. J. A. Koster, "Identification of the dominant recombination process for perovskite solar cells based on machine learning", Cell Reports Physical Science **2** (2021) 100346. https://doi.org/10.1016/j.xcrp.2021.100346.
[62] A. Castro-Chong, A. J. Riquelme, T. Aernouts, L. J. Bennett, G. Richardson, G. Oskam & J. A. Anta, "Illumination intensity dependence of the recombination mechanism in mixed perovskite solar cells", ChemPlusChem **86** (2021) 1347. https://doi.org/10.1002/cplu.202100233.
[63] T. Du, W. Xu, S. Xu, S. R. Ratnasingham, C. T. Lin, J. Kim, J. Briscoe, M. A. McLachlan & J. R. Durrant, "Light-intensity and thickness dependent efficiency of planar perovskite solar cells: charge recombination versus extraction", Journal of Materials Chemistry C **8** (2020) 12648. https://doi.org/10.1039/D0TC03390A.
[64] A. Farokhi, H. Shahroosvand, F. Naderloo, S. Bellani, G. Grancini, A. Di Carlo, L. Manna & M. K. Nazeeruddin, "Low-cost, large-area carbon electrode perovskite solar cells", Journal of Materials Chemistry A **13** (2025) 37700. https://doi.org/10.1039/D5TA05091J.
[65] J. Manit, P. Kanjanaboos, P. Naweephattana, A. Kaewprajak, S. Channarong, T. Supasai, N. Rujisamphan & N. Thongprong, "Towards device stability of perovskite solar cells through low-cost alkyl-terminated SFX-based hole transporting materials and carbon electrodes", Scientific Reports **14** (2024) 24167. https://doi.org/10.1038/s41598-024-74735-4.
[66] S. Ullah, M. Kaleem, F. Khan, A. Nasir & M. Al-Rasheidi, "Design and optimization of highly efficient and lead-free Cs_2TeI_6-based double perovskite solar cells: insights from DFT and SCAPS-1D", Solar Energy Materials and Solar Cells **301** (2026) 114334. https://doi.org/10.1016/j.solmat.2026.114334.